Fall 2021

Simulation and Fabrication of All Oxide-Based ITO/TiO2/CuO/Au Heterostructure for Solar Cell Applications

Sajal Islam
Missouri State University, Sajal123@live.missouristate.edu

SIMULATION AND FABRICATION OF ALL OXIDE-BASED ITO/TiO_2/CuO/Au HETEROSTRUCTURE FOR SOLAR CELL APPLICATIONS

A Master's Thesis

Presented to

The Graduate College of

Missouri State University

In Partial Fulfillment

Of the Requirements for the Degree

Master of Science, Material Science

By

Sajal Islam

December 2021

SIMULATION AND FABRICATION OF ALL OXIDE BASED ITO/TiO_2/CuO/Au HETEROSTRUCTURE FOR SOLAR CELL APPLICATIONS

Physics, Astronomy, and Materials Science

Missouri State University, December 2021

Master of Science

Sajal Islam

ABSTRACT

Oxide heterostructures have drawn great attention lately, due to their environment-friendly properties and potential applications in optoelectronic devices. In this work, a simulation study of a heterojunction solar cell was performed with SCAPS (a solar cell simulator) using TiO_2 as an n-type and CuO as a p-type layer. The thickness and the dopant dependent simulations have shown that the solar cell operates at a maximum efficiency of 19.2% when the thickness of the TiO_2/CuO layers are chosen 1.4µm/1.2µm compared to the 11.5% efficiency when FTO is replaced with ITO. An indium doped tin oxide (ITO) vs fluorine doped tin oxide (FTO) comparison study was carried out where FTO worked better than ITO as a transparent anode electrode in this structure. Gold worked better as a cathode electrode from a range of metallic elements, and it was observed that efficiency increases with the increase in the metal work function. Based on the simulation results, the oxide-based heterojunction was fabricated on ITO substrates using pulsed laser deposition (PLD), spin coating, and sputtering techniques. Structural-property correlations were conducted using x-ray diffraction, Raman spectroscopy, scanning electron microscopy, and electrical measurements i.e., diode characteristics test with light and without light. Rutile phase of TiO_2 was successfully grown on glass, quartz, and ITO to find the best growth parameters for TiO_2 film. Same experimental works were carried out for the CuO layer growth where spin coating, PLD and combination of both techniques were used and compared. Finally, the cathode layer of gold was deposited by the sputtering technique. The solar cell characterization was performed by the I-V measurement using a standard solar simulator and UV-VIS spectroscopy. Origin, Vesta and Mercury software were used for data analysis. It was observed that the devices where the CuO layer was PLD grown has more absorbance of the visible light spectrum. Also, the PLD grown samples worked better, showed an efficiency region in the I-V curve and performed solar characteristics under visible light spectrum.

KEYWORDS: thin films, heterostructure, solar cell, titanium dioxide, copper oxide, indium doped tin oxide, pulsed layer deposition, X ray diffraction, Raman spectroscopy, electrical characterization

SIMULATION AND FABRICATION OF ALL OXIDE BASED ITO/TiO_2/CuO/Au HETEROSTRUCTURE FOR SOLAR CELL APPLICATIONS

By

Sajal Islam

A Master's Thesis
Submitted to the Graduate College
Of Missouri State University
In Partial Fulfillment of the Requirements
For the Degree of Master of Science, Material Science

December 2021

Approved:

Kartik Ghosh, Ph.D., Thesis Committee Chair

Ridwan Sakidja, Ph.D., Committee Member

Tiglet Besara, Ph.D., Committee Member

Julie Masterson, Ph.D., Dean of the Graduate College

ACKNOWLEDGEMENTS

Thanks to the Almighty for all his blessings upon me to be here at MSU, carry out this research work, and complete this thesis.

I would like to thank Dr. Kartik Ghosh, for being so supportive, understanding, considerable, friendly, and inspiring throughout my journey at MSU. I would also like to thank Dr. Ridwan Sakidja and Dr. Tiglet Besara for being cooperate and sharing insightful thoughts on my research.

I would also like to thank Dr. Ariful Haque and Dr. M.F.N. Taufique for being a part of our research group and inspiring me continuously with their knowledge and experience.

Last but not the least, my fellow research teammates Bishwajite Karmakar and Rifat Ara Shams for being there when I needed them.

I dedicate this thesis to those three persons who have dedicated their lives for my success. My mother, my sister, and my wife.

TABLE OF CONTENTS

Introduction Page 1
- Background Page 1
- Theory of a Solar Cell Page 3
- SCAPS-1D: The Solar Simulator Page 4

Simulation Work with SCAPS and Finalization of the Device Structure Page 5
- The Role of the Bottom Contact: Indium Doped Tin Oxide vs Fluorine Doped Tin Oxide Page 6
- Choice of Window and Active Layers Page 6
- Thickness of the P-Type and the N-Type Layers Page 7
- Optimization of the Anode Layer Page 10
- The Finalized Solar Cell Structure Page 12
- Energy Band Alignment Page 13

Experimental Methods Page 14
- Workflow Chart to Fabricate the Glass/ITO/TiO_2/CuO Heterostructure Page 15
- N-Type Layer of TiO_2 Using Pulsed Laser Deposition Technique Page 18
- P-Type Layer of CuO Using Different Deposition Techniques Page 19
- Plasma Etching and Gold Sputtering Page 22

Results and Discussion Page 24
- X-Ray Diffraction (XRD) Page 24
- Raman Spectroscopy Page 30
- Electrical Measurements Page 32
- SEM-EDS Analysis Page 37
- UV-VIS Spectroscopy Page 42

Conclusions and Future Work Page 48

References Page 49

LIST OF TABLES

Table 2.1: TiO_2 and CuO material parameters to feed SCAPS Page 5

Table 2.2: Comparison of ITO with FTO as the bottom contact Page 6

Table 2.3: Thickness dependent simulation to find the CuO layer thickness that gives the maximum efficiency of the solar cell Page 7

Table 2.4: Thickness dependent simulation to find the TiO_2 layer thickness that gives the maximum efficiency of the solar cell Page 9

Table 2.5: Comparison of different materials with various metal work function to find the best top contact Page 11

Table 3.1: The laser parameter used for the pulsed laser deposition technique Page 17

LIST OF FIGURES

Figure 2.1: Effect of the CuO layer thickness on the efficiency of the solar cell — Page 8

Figure 2.2: Effect of TiO_2 layer thickness on the efficiency of the solar cell — Page 10

Figure 2.3: The eight ITO islands on one sample — Page 12

Figure 2.4: The schematic diagram of the solar cell showing the individual layer structure. — Page 12

Figure 2.5: Energy Band alignment of the solar cell — Page 13

Figure 3.1: Schematic of the workflow chart showing the fabrication of the solar cell — Page 15

Figure 3.2: Schematic of a PLD chamber — Page 18

Figure 3.3: The 0.05M CuO solution made from CuO bulk powder. — Page 21

Figure 3.4: The spin coater used to spin coat the CuO layer. — Page 21

Figure 4.1: XRD analysis of the PLD grown TiO_2 samples on glass substrate. — Page 25

Figure 4.2: XRD analysis of the PLD grown TiO_2 samples on quartz substrate. — Page 26

Figure 4.3: XRD analysis of the Cu, CuO, Cu_2O cif files — Page 27

Figure 4.4: XRD analysis of the spin coated CuO layer on glass substrates. — Page 28

Figure 4.5: XRD analysis of the ITO substrate. — Page 28

Figure 4.6: XRD analysis of the glass/ITO/TiO_2 layer — Page 29

Figure 4.7: XRD analysis of the complete glass/ITO/TiO_2/CuO solar cell — Page 30

Figure 4.8: Raman spectroscopy of the PLD grown TiO_2 samples on quartz substrate. — Page 31

Figure 4.9: Raman spectroscopy of the PLD grown TiO_2 samples on ITO Page 32

Figure 4.10: Electrical measurement setup diagram. (Components are not to scale.) Page 32

Figure 4.11: Standard diode characteristics (I-V measurement) Page 33

Figure 4.12: Diode characteristics (I-V) measurement of the solar cell (Type 1 Sample) Page 34

Figure 4.13: Diode characteristics (I-V) measurement of the solar cell (Type 2 sample) Page 35

Figure 4.14: Diode characteristics (I-V) measurement of the solar cell (Type 2 sample) Page 35

Figure 4.15: Diode characteristics (I-V) measurement of the solar cell (Type 2 sample) Page 36

Figure 4.16: Diode characteristics (I-V) measurement of the solar cell (Type 2 sample) Page 37

Figure 4.17: Diode characteristics (I-V) measurement of the solar cell (Type 3 sample) Page 38

Figure 4.18: Diode characteristics (I-V) measurement of the solar cell (Type 3 sample) Page 38

Figure 4.19: SEM image of PLD grown solar cell (Type 2 sample) Page 39

Figure 4.20: EDS image of the PLD grown solar cell showing the distributed presence of all the materials Page 40

Figure 4.21: EDS data showing the presence of all the materials in the sample. Page 41

Figure 4.22: SEM image of PLD grown solar cell with a CuO spin coated layer (type 3 sample) Page 42

Figure 4.23: EDS image of PLD grown solar cell with a CuO spin coated layer (type 3 sample) showing the distributed presence of all the materials Page 43

Figure 4.24: UV-VIS spectroscopy comparison between each layer of the glass/ITO/TiO_2/CuO (type 1 sample) solar cell Page 44

Figure 4.25: UV-VIS spectroscopy comparison between each layer of the glass/ITO/TiO_2/CuO (type 2 sample) solar cell Page 45

Figure 4.26: UV-VIS spectroscopy comparison between each layer of the glass/ITO/TiO_2/CuO (type 1 sample) solar cell Page 46

Figure 4.27: Absorbance spectrum of each layer of the solar cell sample Page 46

INTRODUCTION

Background

Solar power is one of the most significant sources of renewable energy on the planet that has the potential to alleviate the global energy issue in the future.[1] The photovoltaic (PV) device industry is rising at a rapid pace worldwide.[2] Fabricating high efficiency solar cell with cost effective unique techniques is in grave need to fulfill the ever-increasing energy demand.[3] The traditional photovoltaic (PV) devices standing on the theory of a p-n junction diode, has been challenged lately with numerous reports of solar-electric energy conversion concept.[4] In a solar cell, the semiconductor materials are primarily chosen based on their band gap, optical properties and charge carrier diffusion length.[5,6] Metal oxides (MO) semiconductors, which are inexpensive, chemically stable, and environmentally benign are suitable candidates for photoelectric devices with their advantage of ambient conditions material deposition.[7,8]

A high efficient solar cell demands a high band gap n-type semiconductor material for the window layer to pass the maximum possible amount of light through it and a narrow band gap p-type semiconductor material for the optically active photovoltaic layer to perform nearly complete light absorption.[3] Although the absorption of the visible solar spectrum can be increased by growing a thicker p-type layer however, this can cause an exceeding electron diffusion length through the network of the nanoparticles leading to a destructive effect on the device.[9] Hence, it is highly significant to determining the optimum layer thickness in a solar cell structure for both the p-type and the n-type layer to absorb the maximum visible light spectrum and convert it into the highest electrical energy.

Titanium dioxide (TiO2) has sparked a lot of attention in the last few years due to its application in solar energy, photovoltaic devices, integrated wave guides, photocatalyst, and medicine[10] It is a white solid inorganic metal oxide substance, thermally stable, non-expensive and non-flammable, poorly soluble, non-hazardous and naturally found in rocks and mineral sands.[11] As titanium dioxide is transparent in the region of the visible and infrared spectral and absorbs the ultraviolet spectrum, it is highly useful for optical applications.[12] Although there are several shapes of titanium dioxide such as powder, bulks and thin films, the last one is the suitable one for photocatalyst application.[13] So far, various techniques have been reported to synthesize titanium dioxide thin films such as coating, chemical vapor deposition, sputtering, anode oxidation, and pulsed laser deposition (PLD), however, the properties of the deposited thin film can be easily modified through adjusting the operating parameters made PLD a suitable choice for researchers.[13] Rutile (tetragonal), anatase (tetragonal), and brookite (orthorhombic) are the three crystallographic structures of titanium dioxide while rutile is the most stable phase of titanium dioxide and also found in nature.[12] Synthesizing the rutile phase of titanium dioxide is easier than synthesizing the anatase phase because of its more thermodynamic stability.[14]

As a p-type, narrow band gap, photovoltaic material, copper oxide based semi-conductors are extensively studied.[15] Due to its plentiful presence in nature and suitable optical properties in the solar cell application,[3] copper oxide has myriad number of literature reports in a photovoltaic heterostructure frequently arranged by utilizing low-cost, solution-based techniques.[16–18] Environment friendly, great prevalence, a relatively easy preparation technique, and individual square planar coordination of copper and oxygen are only a few of the advantages of copper oxide.[19,20] Cupric oxide (CuO) and cuprous oxide (Cu_2O) are

the two stable forms of copper oxide that are categorized as transitional metal oxide semiconductors.[21–23] While CuO is black, has monoclinic crystal structure and a bandgap of 1.0-2.1 eV,[24,25] Cu_2O has a cubic crystal structure and a bandgap of 2-2.6 eV.[26] As a p-type semiconductor material, both cupric oxide (CuO) and cuprous oxide (Cu_2O) are widely used for solar cell applications.[27,28] So, it is exceptionally important to know the effect of CuO and Cu_2O on the efficiency of a solar cell heterostructure. Previously, copper oxide based thin film solar cell has reported an efficiency of 2.9% with ZnO as an n-type material.[3]

There are a wide variety of device structures proposed in the literature which includes absorbing thin film layers embedded with nanopillar collectors,[29] and nanopillar arrays that has axial and radial junctions.[30–32] To achieve better optical properties for metal oxides, bandgap engineering is also reported by doping[33] and mixed oxide synthesis.[34] For understanding the charge transport at the junction of the layers, it is also important to understand the relative band alignment of the two semiconductor materials. A type II or a type III band alignment is necessary to have an effective breach between the charge carriers.[35] Furthermore, the p-type material should have higher valence and conduction bands than the n-type material for a superior charge transport in thin films.[3] Therefore, the band alignment formed by the titanium dioxide with copper oxide makes it a perfect choice for the solar cell application.

Theory of a Solar Cell

Sola cell, also known as photovoltaic device, works on the principal of photovoltaic effect. It is such a device that converts the light energy to electrical energy when light is exposed on the cell. A solar cell consists of mainly a p-type material, a n-type material, a top and a bottom contact. When a solar device is exposed to light, it can absorb the light energy at the

same time reflect and pass through it. The purpose of the n-type and the p-type material is to create the p-n junction where light can be exposed, they can convert the light directly to electricity. The n-type material in a solar cell is also known as the window layer because it allows the light to pass through it. So, the n-type material must be a wide band gap semiconductor. The p-type material in a solar cell is known as the absorber layer. So, it must be a narrow band gap material so that it can absorb light more.

In a p-n junction of a solar cell when light is shined the electrons can absorb the photon energy and electron-hole pairs are formed in the depletion region. As a result, positive and negative charges accumulate, and a voltage difference is created. This is the photovoltaic effect. This voltage difference creates a continuous flow of electricity which is the working principal of a solar cell.

SCAPS-1D: The Solar Simulator

Researchers have been using different simulation software and numerical solution packages, such as AMPS-1D, ASPIN, AFORS-HET, AND SCAPS-1D. SCAPS-1D is a one-dimensional solar cell simulator program that allows to do simulation run of solar cell made with different materials. The simulation can be performed under a variety of spectrum and materials comparison for the solar cell layers as well as thickness measurement for each layer can be carried out with SCAPS. The program is developed at ELIS, University of Gent, and the most recent version of the SCAPS 3.8, released in May 2020 was used to perform the simulation work.

SIMULATION WITH SCAPS AND FINALIZATION OF THE DEVICE STRUCTURE

The SCAPS has a user-friendly interface where one can provide the known parameters of a material and make an individual layer. In the same was all the other layers can be created, and the solar cell can be simulated to find the efficiency of the solar cell. The following parameters of TiO_2 and CuO were fed to SCAPS to run the simulation which is shown in the Table 2.1. The parameters were taken from the literature.

Table 2.1: TiO_2 and CuO material parameters to feed SCAPS[2,36–38]

Parameters	CuO	TiO_2
Thickness (μm)	1.2 μm	1.4 μm
Bandgap (eV)	1.51	3.2
Electron Affinity (eV)	4.07	4.2
Dielectric Permittivity (relative)	18.1	10
CB effective density of states (1/cm^3)	2.20E+19	2.00E+18
VB effective density of states (1/cm^3)	5.50E+20	1.80E+19
Electron thermal velocity (cm/s)	1.00E+07	1.00E+07
hole thermal velocity (cm/s)	1.00E+07	1.00E+07
Electron mobility (cm^2/Vs)	1.00E+02	1.00E+02
hole mobility (cm^2/Vs)	1.00E-01	2.50E+01
Shallow uniform donor density ND (1/cm^3)	0.00E+00	1.00E+17
Shallow uniform acceptor density ND (1/cm^3)	1.00E+16	0.00E+00

Using the above parameters, several simulations were carried out with SCSAPS. 1. ZnO was compared with TiO_2 as the window layer. 2. CuO was compared with Cu_2O as the absorber layer. 3. ITO was compared with FTO as the bottom contact. 4. Gold was compared with several other materials as the top contact. 5. Thickness dependent simulation was carried out for the window and the absorber layer.

The Role of the Bottom Contact: Indium Doped Tin Oxide vs Fluorine Doped Tin Oxide

For the bottom contact of the solar cell, indium doped tin oxide (ITO) was compared with fluorine doped tin oxide (FTO) using SCAPS. All the other layers and thickness of those layers were kept constant while running these comparison simulations. It was observed that the fluorine doped tin oxide (FTO) increases the efficiency of the solar cell (table 2.2). While indium doped tin oxide (ITO) gives 11.5% efficiency, with the fluorine doped tin oxide (FTO), the solar cell performs with a 22.4% efficiency.

Table 2.2: Comparison of ITO with FTO as the bottom contact

Left contact with TiO_2/CuO/Au structure	Efficiency
ITO	11.5%
FTO	22.4%

Choice of Window and Active Layers

A solar cell needs an n-type material and, a p-type material for the p-n junction to create voltage difference upon exposure of sun light. It also needs a transparent bottom contact and a top contact to maintain the electron flow to create electricity. The n-type material, also known as the window layer, must be a wide band gap material so that it can allow the light spectra to pass

through it. On the other side the p-type material, also known as the active layer of a solar cell, needs to be a narrow band gap material so that it can absorb most of the spectra. The bottom contact must be transparent and thin to transmit light spectra through it. For the buffer layer of the solar cell TiO_2 was compared with ZnO, and it was observed in the simulation that TiO_2 works better than ZnO as a wide band gap semiconductor. Similar comparison was carried out for the absorber layer with CuO and Cu_2O and it was observed from the simulation that the CuO works better than Cu_2O as the narrow band gap material.

Thickness of the P-Type and the N-Type Layers

Thickness dependent simulation study for the p-type CuO layer was carried out with SCAPS (table 2.3). While all other parameters were kept constant, only the CuO layer thickness was varied.

Table 2.3: Thickness dependent simulation to find the CuO layer thickness that gives the maximum efficiency of the solar cell.

Thickness of CuO (μm)	Efficiency (%)
0.5	18.0
1	19.0
1.1	19.1
1.25	19.1
1.31	19.1
1.35	19.1
1.4	19.1
1.5	19.0
2	18.9
2.5	18.7

With varying thickness, the change in efficiency of the solar cell was observed. Table 2.3 shows the effect of CuO layer thickness on the solar cell efficiency. The thickness was varied from 0.5 µm to 2.5 µm and it was observed that the solar cell performs with best efficiency of 19.1% at the thickness of CuO layer from 1.1 µm to 1.31 µm shown in the figure 2.1.

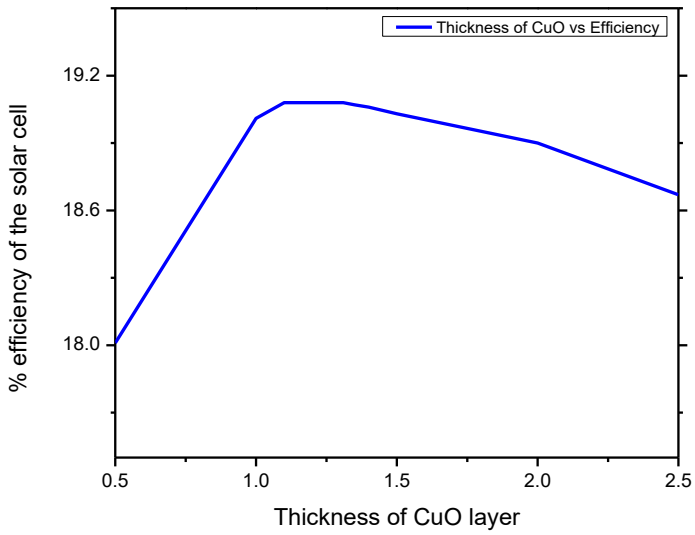

Figure 2.1: Effect of CuO layer thickness on the efficiency of the solar cell

Study of thickness dependent simulation was also carried out with SCAPS. Keeping all the layers unchanged, the thickness of TiO_2 layer was varied and the effect of different thickness on the solar cell was determined through simulation with SCAPS. Table 2.4 shows the effect of TiO_2 layer thickness on the solar cell efficiency. The thickness was varied from 0.1 µm to 2 µm and it was observed that the solar cell performs with best efficiency of 19.2% at the thickness of TiO_2 layer from 1.3 µm to 1.5 µm.

Table 2.4: Thickness dependent simulation to find the TiO_2 layer thickness that gives the maximum efficiency of the solar cell.

Thickness of TiO_2 (μm)	Efficiency (%)
0.1	19.1
0.5	19.1
1	19.1
1.2	19.1
1.3	19.2
1.4	19.2
1.5	19.2
1.6	19.1
1.8	19.1
2	19.1

The figure 2.2 depicts the simulation results from SCAPS that shows the thickness effect of TiO_2 layer on the solar cell efficiency. Varying the thickness from 0.1 μm to 2 μm it was observed that the solar cell performance increases and maximizes at the thickness of TiO_2 layer from 1.3 μm to 1.5 μm. The maximum achievable efficiency from this structure with this thickness is 19.2%

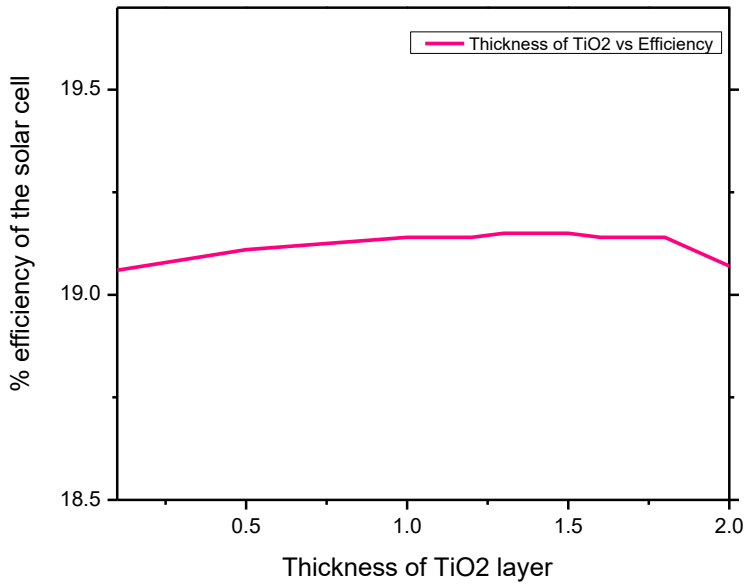

Figure 2.2: Effect of TiO_2 layer thickness on the efficiency of the solar cell

Optimization of the Anode Layer

To choose the top contact of the solar cell, different materials were used and tested using SCAPS with a variety of metal work function as shown in the table 2.5. It was found that the solar cell efficiency increases proportionally with a material that has a higher metal work function. Also, it was observed that the simulation ends up showing error with any material with a metal work function less than 4.5 eV. The solar cell performs best with a 5.1 metal work function material, gold and gives the highest efficiency of 19.6%.

Based on the simulation work results, it was decided that an all oxide-based glass/ITO/TiO_2/CuO heterostructure would be fabricated and tested experimentally and the results would be compared with the simulation results. The first challenge was to deposit each layer and figure out the quality and phase of the deposited materials. The second challenge was

Table 2.5: Comparison of different materials with various metal work function to find the best top contact.

Element	Work Function(eV)	Efficiency
Aluminum	4.08	Error
Lead	4.14	Error
Niobium	4.3	Error
Zinc	4.3	Error
Iron	4.5	3.8%
Copper	4.7	8.7%
Carbon	4.81	11.5%
Nickel	5.01	16.8%
Gold	5.1	19.6%

to fabricate the solar cell itself and finally to characterize it for solar characteristics. The following figure 2.3 shows the ITO substrate used to synthesize the glass/ITO/TiO_2/CuO heterostructure layers of the solar cell. Each ITO substrate has 8 islands which allows to make 8 separate solar cells.

Figure 2.3: The eight ITO islands on one sample

The Finalized Solar Cell Structure

Figure 2.4 represents the schematic diagram of the solar cell that was finalized by the simulation study. The bottom layer is the transparent glass with transparent ITO on top of it. A special type of glass/ITO substrates were bought on which 8 solar samples can be fabricated at the same time. The next layer is the n-type material TiO_2 layer followed by a p-type material CuO layer. It was decided that the TiO_2 layer would be grown by the PLD technique and the CuO layer would be grown by PLD, spin coating and a mixture of these two techniques. Finally

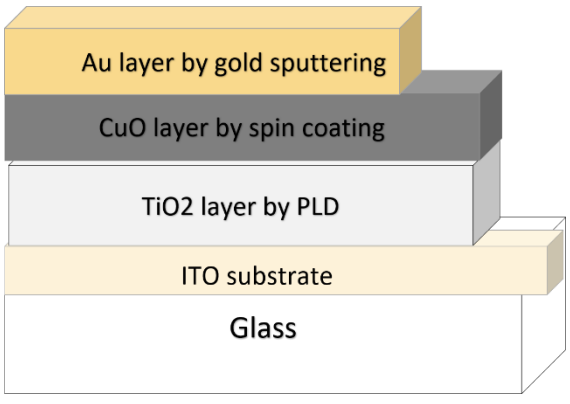

Figure 2.4: The schematic diagram of the solar cell showing the individual layer structure.

comes the Au layer which would be fabricated by sputtering technique.

Energy Band Alignment

The following figure 2.5 shows the energy band alignment diagram of the proposed solar cell. From the figure it can be visualize how electrons can easily flow from CuO to TiO_2 to FTO and how holes can easily flow from TiO_2 to CuO to Au. Just as the water flows from higher level to lower level, the band alignment diagram also shows the flow of electrons and holes. The numbers in the figure are in electron volt unit.

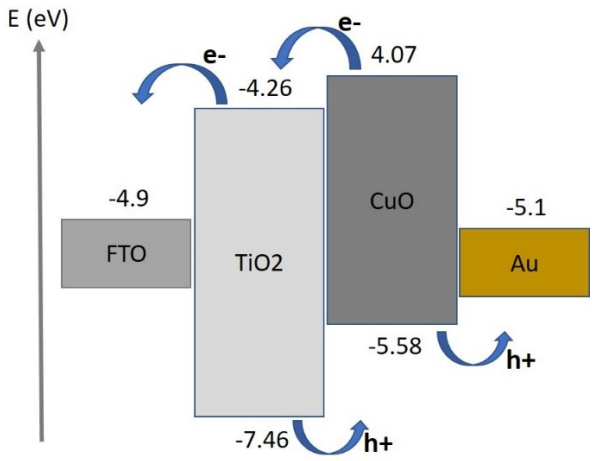

Figure 2.5: Energy Band alignment of the solar cell

EXPERIMENTAL METHODS

The figure 3.1 is a visual representation of the workflow to fabricate each solar cell. First the ITO substrate was masked on both sides with aluminum foil, and TiO_2 was deposited. It allows to have access of the ITO even after the deposition. Same aluminum mask is used to grow CuO by PLD for some of the samples. The samples where spin coating is used to deposit CuO, parafilm mask is used to cover the ITO contacts tightly from the CuO solution touching it. After this, thick paper mask is used to cover both sides again, and Au sputtering was done for the Au layer.

An extensive experimental work was done and a huge number of TiO_2 samples were grown using the pulsed laser deposition (PLD) techniques. Hence, it is important to talk about the PLD parameters, synthesis process and how that effects the growth of TiO_2 samples on different substrates. The target solar cell structure was glass/ITO/TiO_2/CuO/Au, which means the TiO_2 must be grown on ITO substrate. However, we have used four different substrates to study the TiO_2 growth. These substrates are 1) glass, 2) quartz, 3) SiO2 and 4) ITO. We did literature review on TiO_2 growth and used those parameters as the first steppingstone. We started with glass as a substrate to grow TiO_2 thin films because of two reasons. 1) The ITO substrate we were about to use was also on glass. So, the growth parameter that works on plain glass substrates should also work on those ITO substrates. 2) The glass substrates are cheaper than the ITO substrates. So, initial works with glass instead of ITO can reduce the overall research expense. Then we used Quartz substrates to deposit TiO_2 because 1) quartz is more robust that glass and 2) it gives more liberty to play with different PLD growth parameters i.e., temperature. 3) Quartz substrate is also cheaper than the ITO substrate. We also used Si as a substrate for

Workflow Chart to Fabricate the Glass/ITO/TiO_2/CuO Heterostructure

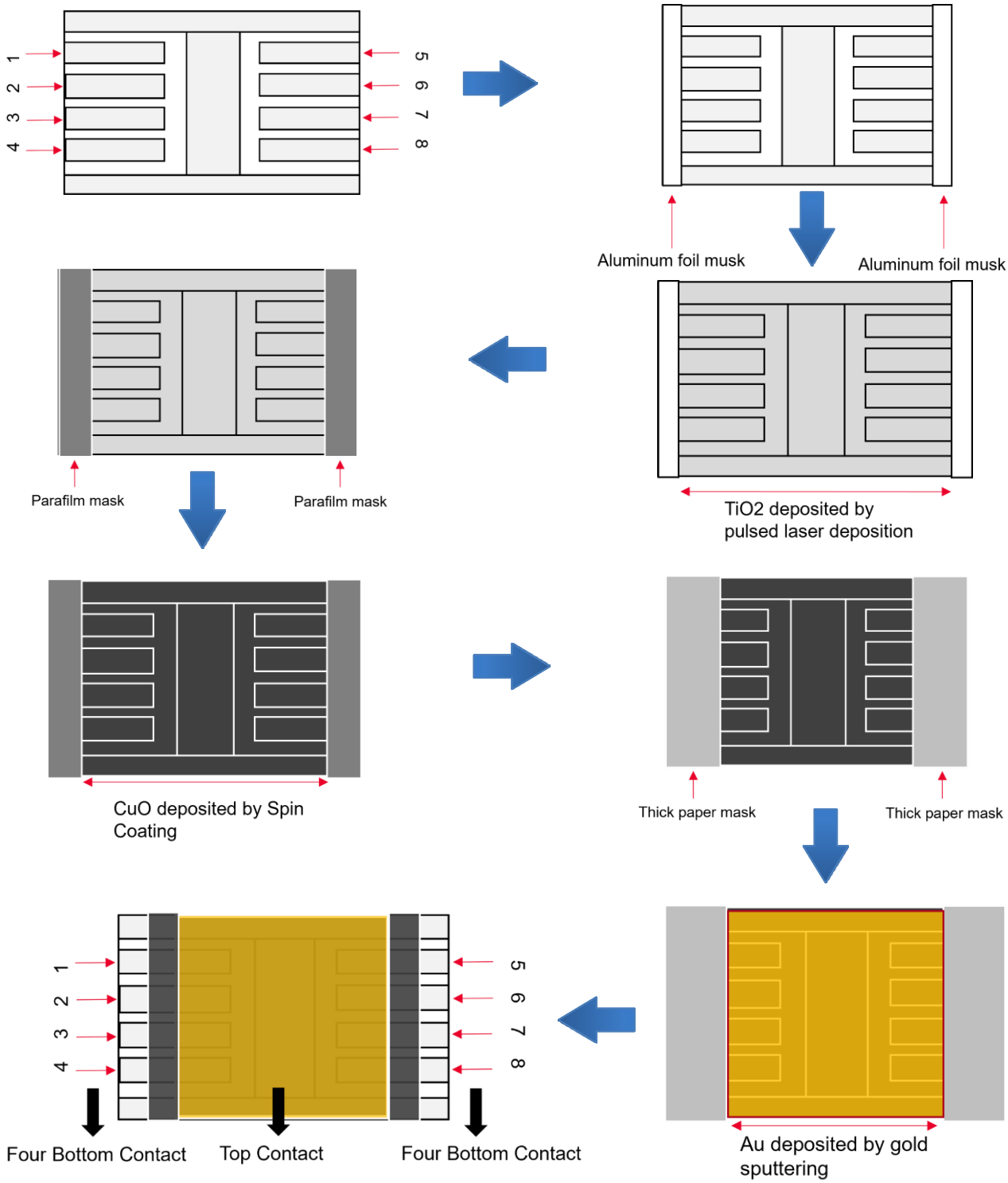

Figure 3.1: Schematic of the workflow chart showing the fabrication of the solar cell

TiO_2 deposition because 1) it is easier to do Raman studies to find TiO_2 peaks as Si has a prominent Raman Peak at 520 cm^{-1}. 2) Another cheaper substrate which can reduce initial research cost. Finally, we have used glass/ITO substrates to get the desired TiO_2 thin film deposition. All these substrates allowed us to study and find the growth parameters using PLD that can be used to deposit grow good quality TiO_2 thin films.

The titanium dioxide (TiO_2) thin films were deposition on different substrates via pulsed laser deposition was performed in a 12 spherical vacuum chamber. The chamber consists of the following main components: Gas inlet valve, focusing lens, port with quartz window, substrate holder/heater, pressure gauge, target holder/carousel, roughing pump, and turbo-molecular pump. The figure 3.2 shows the schematic of a PLD chamber.

Before each deposition, the substrate was properly cleaned in a sonication bath with Methanol for 20 minutes. This step was skipped only for the ITO samples. Instead of sonication bath, the ITO samples were washed directly with Methanol. The upper surface of the substrate holder, substrate holding pins and screws were properly rubbed with sandpapers to remove any leftover deposited material from the previous deposition. The titanium target is also rubbed with sandpaper to clean and smoothen the surface. After rubbing those equipment parts were cleaned with tissue papers wet in Methanol followed by dry tissue papers. The inside of the chamber and the rubber gasket between the chamber and the substrate holder was also cleaned with wet and dry tissue papers. Then the substrate was put on the substrate holder and tied with pins in the proper spot where the maximum amount of TiO_2 from the target can reach while deposition. The laser main switch is turned on at this point and it takes some time for the laser machine to get ready for laser shots. The titanium target was mounted inside the chamber and tied with a screw

to stop any movement while deposition. Using the small laser monitor, the laser parameters were set.

For the pulsed laser deposition technique, a neodymium-doped yttrium aluminum garnet (ND:YAG) nanosecond pulsed laser was used. The following table 3.1 shows the parameters used in the laser for the titanium dioxide deposition. The FL – Q – Switch delay was increased to get less amount of laser energy while setting up the carousal and finding the best position for the substrate.

Table 3.1: The laser parameters used for the pulsed laser deposition technique

Voltage	Pulse Width	Flash lamp repetition rate	Q Switch repetition rate	Q Switch divider F/N	Q – switch out synchronization	FL – Q – Switch delay
681 V	175 µs	10 Hz	10 Hz	1	10 ns	10 µs

The figure 3.2 represents the schematic of the PLD chamber used. The spot size of the laser beam was measured in a specific way. After the laser alignment was done and the laser parameters were set, a small piece of thermal paper was attached on the target with a double-sided tape. Then the paper was shot with a one singe laser beam. This makes a black dot on the paper surface which tells us the laser beam spot size. The diameter of the spot was measured to determine the spot size. The laser spot was oval shaped with a diameter of 1.2 mm on the longer side and 0.8 mm on the shorter side which makes the spot size an average diameter of ((1.2+0.8)/2) = 1 mm.

The energy density is another crucial parameter for pulsed laser deposition. After the spot size was measured and found 1 mm in diameter, the laser energy was measured with the Coherent® FieldMaxII-P Laser Energy Meter. The laser energy was found and varied from 34mj

to 50mj just outside the chamber by varying the above-mentioned laser parameters. The following equation was used to determine the energy density. The energy density was varied from 4.33 J/cm^2 to 6.37 J/cm^2.

$$Energy\ Density = \frac{Laser\ energy}{Area\ of\ the\ laser\ spot}$$

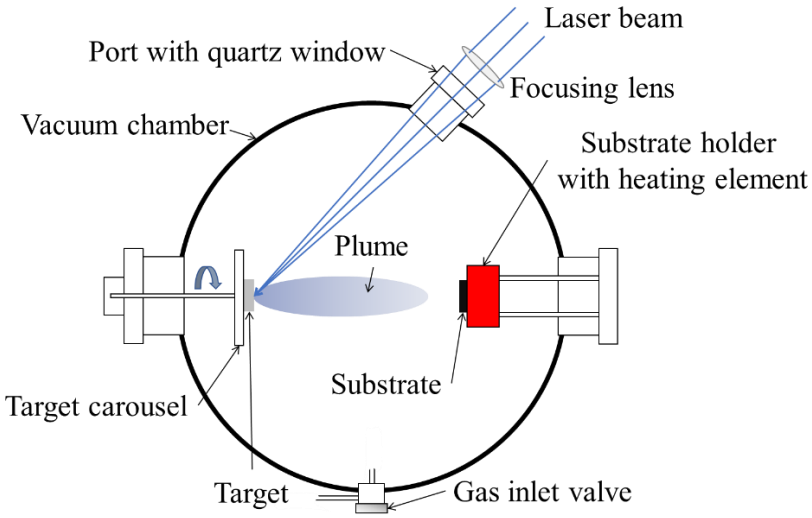

Figure 3.2: Schematic of a PLD chamber.

N-Type Layer of TiO_2 Using Pulsed Laser Deposition Technique

After all the above steps, the target was put carefully inside the PLD chamber. The substrate was mounted on the substrate holder and tied with the substrate pins. The chamber is then closed and pumped down to a base pressure of 5.0E-5 to 5.0E-6 mbar with the help of a roughing and a turbo molecular pump. This base pressure was achieved to eliminate all other impurities that might be inside the chamber along with environmental gases and moistures. After reaching the desired base pressure, the pump's standby mood was turned on. With 30% to 40% of the full running frequency of 833Hz of the pump, the desired deposition pressure can be easily

reached and kept steady. Once the pump starts running in the standby frequency, the temperature controller was turned on to heat the substrate inside the chamber with a 30-minute ramp time to reach the desired temperature. For different depositions, the temperature was varied within a range of 400^0 C to 600^0 C. As soon as the deposition temperature was reached the gate valve was nearly closed and O^2 gas inlet valve was opened to introduce O^2 gas to the chamber. The O^2 gas flow was controlled by a needle valve to keep the pressure inside the chamber steady. This caused the pressure increase inside the PLD chamber to 1.1E-1 mbar. At this point laser was turned on. Initially the target was shot hit with 20,000 laser shots to grow TiO_2 thin films on different substrates like glass, quartz, and silicon. When the solar cell samples were made on ITO substrates, 30,000 laser shots were given to the target. Extra 500 shots were used on every deposition to ablate and clean the surface of the titanium target. While doing the deposition, the chamber pressure was kept constant at 1.1E-1 mbar for the whole time. The Ti target gets ablated by the laser shot and keeps deposited under to O_2 atmosphere inside the chamber and creates TiO_2 thin film layer on the ITO substrate. After every deposition was done, more O_2 was put inside the chamber to go the O_2 pressure as high as 250 mbar. In this stage the sample was annealed inside the same chamber in O_2 atmosphere for 10 minutes with the same deposition temperature of 400^0 C to 600^0 C. After annealing the thin film was naturally cooled down to room temperature before taken out of the chamber.

P-Type Layer of CuO Using Different Deposition Techniques

To make the heterostructure of glass/ITO/TiO_2/CuO, after the glass/ITO/TiO_2 layer, spin coating was used in some of the samples to make the CuO thin film layer and pulsed laser deposition was used to make some other samples while both the techniques were used

simultaneously for the rest of the samples. The characterizations of those samples compare and determine the best technique for this heterostructure for solar cell application.

Two targets were used in succession for the second layer of the solar cell which is the p-type material CuO. The identical procedure was followed here as well with just one more target of Cu inside the PLD chamber. After going through the same preparation stage which is the cleaning process for the target, substrate holder and substrate, the same laser parameters were set and the spot size along with the energy density were measured. At this point, instead of one target, both the Ti and the Cu target were put inside the chamber. The ITO substrate was carefully mounted on the substrate holder and perfectly tied with the pins. The chamber was closed after that and using the roughing pump and the turbo molecular pump, the chamber was vacuumed to a base pressure of 5.5E-5 mbar. After this the pump was set to the standby mood for the rest of the process and was running at 30% of its full capacity of 833 Hz. The temperature controller was then turned on and was set to reach the temperature of 400^0 C with a 30 min ramping time. After reaching at 400^0 C the chamber was introduced with O^2 gas which increased the pressure to 1.1E-1 mbar. The carousal was set in a way to give 30,000 laser shots hit the Ti target followed by 40,000 laser shots hit the Cu target with 500 extra shots on each target to clean their surface. This process ablates the Ti and Cu targets respectively under the O2 gas atmosphere and deposits an n-type layer of TiO_2 thin film followed by a p-type layer of CuO thin film on the ITO substrate creating the glass/ITO/TiO_2/CuO heterostructure. After the thin film deposition was done, the sample was annealed in 400^0 C temperature under O2 gas pressure of 250 mbar for 10 minutes inside the same PLD chamber. The sample was then cooled naturally to reach the room temperature before taking it out from chamber.

To do the spin coating for the CuO layer, The Laurell WS-400B-6NPP/Lite Spin coater was used. First a 0.05M CuO solution (figure 3.3) was made by mixing 5g of DI water with 0.02g of CuO powder for using in the spin coater (figure 3.4) as the liquid solution.

$$\text{Molarity of a solution} = \frac{Moles\ of\ solute}{Liters\ of\ solution}$$

$$\text{Here, Moles of CuO solute} = \frac{CuO\ used\ in\ grams}{Molar\ mass\ of\ CuO} = \frac{0.02\ g\ of\ CuO}{79.545\ g/mol} = 2.51\text{E-}4\ \text{mol}$$

$$\text{Hence, the molarity of the solution} = \frac{2.51E{-}4\ mol}{5E{-}3\ \ L} = 0.05\ \text{M}$$

Figure 3.3: The 0.05M CuO solution made from CuO bulk powder.

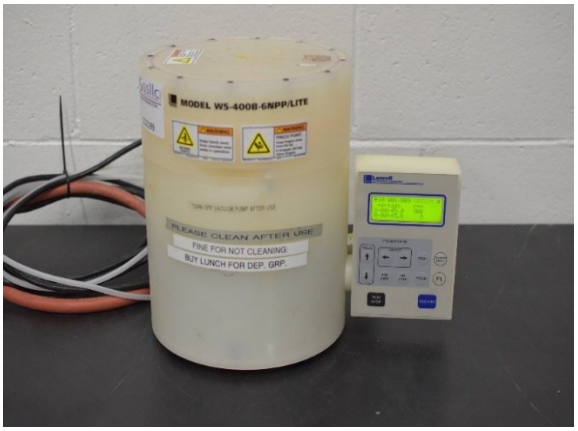

Figure 3.4: The spin coater used to spin coat the CuO layer.

After the 0.05M, CuO solution was made, the glass/ITO/TiO_2 sample was placed inside the spin coater. A dropper was used to put 8-10 drops of 0.05M CuO solution on the glass/ITO/TiO_2 sample to cover the whole surface. Then the lid of the spin coater was closed, and the spinning was started. A preset program that starts the spinning at 200 rpm for 10 seconds followed by a 2000 rpm for a minute and finally at 50 rpm for 5 seconds was used to create the p-type CuO layer. Every time spin coating was performed, this same program was used.

After one layer of CuO thin film was deposited on the substrate, it was heated for 10 minutes in 100^0 C temperature in a furnace under atmospheric pressure and gases. After that the same spin coating procedure was followed to create another layer of CuO followed by furnace heating until the desired number of CuO layers were formed. After the final layer, the sample was heated at 400^0 C for 5 hours in the same furnace in environmental gas pressure and atmosphere.

As a substrate, glass was used initially to check the quality of the CuO thin film, and the spin coated layers were varied from 1 to 5 layers to find out how many layers works best. Finally, glass/ITO/TiO_2 samples were used to make the glass/ITO/TiO_2/CuO heterostructure where 3 layers of spin coated CuO was used. For those samples where both the TiO_2 and CuO thin film layers were grown by the pulsed laser deposition technique, this same spin coating method and spin coating program was used for the added 3 spin coated layer of CuO.

Plasma Etching and Gold Sputtering

To clean the top surface of the glass/ITO/TiO_2 samples, to remove any organic particles and to change them from hydrophobic to hydrophilic, plasma etching was done on every

samples. During the making of each solar cell sample, after the TiO_2 layer, plasma etching treatment was carried out couple of minutes using the Pie Scientific Tergeo Plasma Cleaner.

The final layer of the heterostructure was the gold layer for which gold sputtering technique was used. After the glass/ITO/TiO_2/CuO structure was made, the sample was masked with thick paper in a way that both the sides are covered completely with a little region in the middle remains unmasked. This allows to cover the 8 ITO contacts on the sample from both sides and covers a little area of the ITO islands where TiO_2 and CuO were deposited. The sputtering chamber was vacuumed before the sputtering process was started. Then the gold sputtering was done for 120 seconds. After that, the vacuum was broken, and the complete heterostructure solar cell sample was taken out. The mask was removed carefully, and the solar samples were ready for characterization.

RESULTS AND DISCUSSION

X-Ray Diffraction (XRD)

X- ray diffraction (XRD), a nondestructive characterization technique, was used to determine the layer morphology and the crystal structure. We used XRD as a means for characterization to study the morphology of the layers, especially the n-type and the p-type layer morphology and their crystal structures. The X-ray diffractometer that was used is called a Bruker AXS D8 ADVANCE with a Cu-Kα source which has a wavelength of 1.5406Å. A θ-2θ scan was performed for a range of 20° – 80° in most cases and from 10^0 to 90^0 in some cases. The scan speed was set to 2 seconds with a step size of 0.0196. Phi scan and Z-scan were performed each time to find the Z-value and Phi value of the deposited samples to compensate for the substrate thickness. We performed an XRD scan for all substrates, after every PLD deposition for n-type layer, after every deposition of p-type layers and after the Au layer. To analyze the XRD data, we have used the TOPAS software to perform the Rietveld refinement. We have used the Origin software to delineate the figures accumulated from TOPAS data. To find the crystal structure from the XRD data, we have used sheerer equation. According to the

$$\tau = \frac{K\lambda}{\beta cos\theta}$$

equation

In this equation,

T= crystallite size

K= dimensionless shape factor, its value is close to unity

i.e., 0.9B= Full-width half max θ= Bragg angle

(Bruker, D8 Discover;).

The figure 4.1 shows the graphs of the XRD data plotted by origin. The bottom black graph represents the glass substrate, and the above graphs represent the TiO_2 samples grown on glass. As glass is amorphous, there is no peak present in the XRD plot. The TiO_2 samples grown on glass showed no peak as well which concludes that the deposited material on the glass was amorphous TiO_2. Apart from glass substrates, quartz substrates were also used to grow TiO_2.

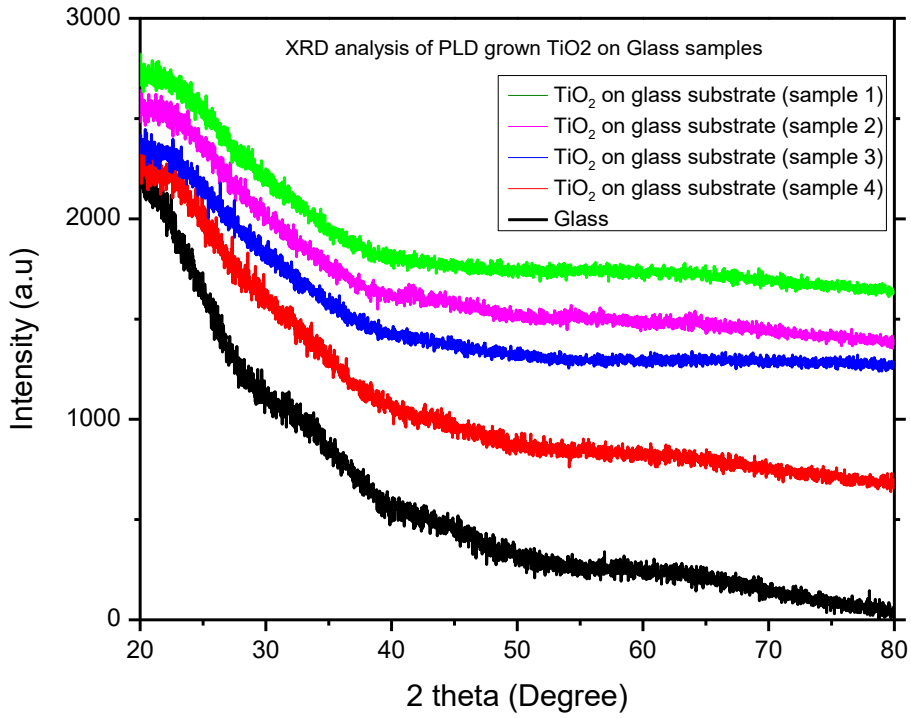

Figure 4.1: XRD analysis of the PLD grown TiO_2 samples on glass substrate.

The following figure 4.2 represents the TiO_2 samples grown on quartz substrates by pulsed laser deposition. The XRD data reveals that the deposited TiO_2 has both rutile and anatase phases present in it. The diffraction peaks present at 27.89^0, 36.38^0, 39.66^0, 41.64^0, 44.39^0, 56.85^0, 64.26^0, and 69.0^0 are assigned to the R(110), R(101), R(200), R(111), R(210),

R(220), R(310), and R(301) lattice plane reflections of tetragonal rutile phase of TiO_2 respectively. The peaks at 54.79^0, and 70.1^0 are coming from the A(105) and A(220) tetragonal anatase phase of TiO_2. Comparatively, there are lot more rutile phase present than anatase phase. So, the grown TiO_2 is mostly rutile which is also the most stable phase for TiO_2.

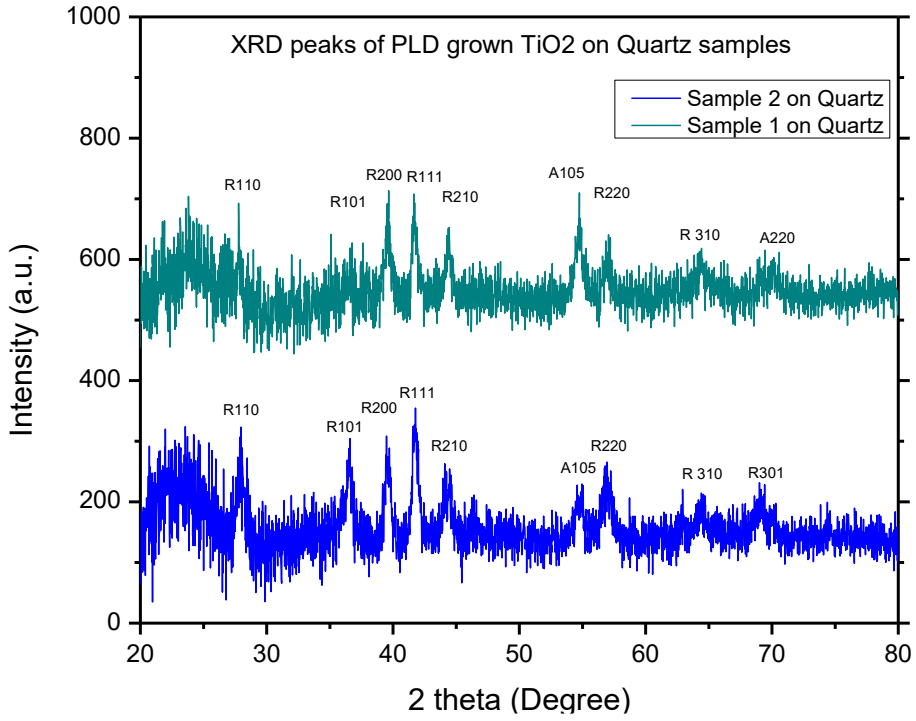

Figure 4.2: XRD analysis of the PLD grown TiO_2 samples on quartz substrate.

The figure 4.3 shows the XRD peaks present in the Cu, CuO and Cu_2O from 20^0 to 80^0. The three cif files[39–41] were downloaded and plotted on origin to match with the peak positions of the grown CuO samples. The Cu graph shows that the peaks are present at (111), (002), and (022) plane. The Cu_2O shows peaks at (011), (111), (002), (112), (022),

(113), and (222) plane whereas for CuO, XRD peaks appear at (110), (002), (11-1), (111), (200), (11-2), (20-2), (112), (020), (021), (202), (11-3), (022), (31-1), (310), (31-2), (004), and (023) plane.

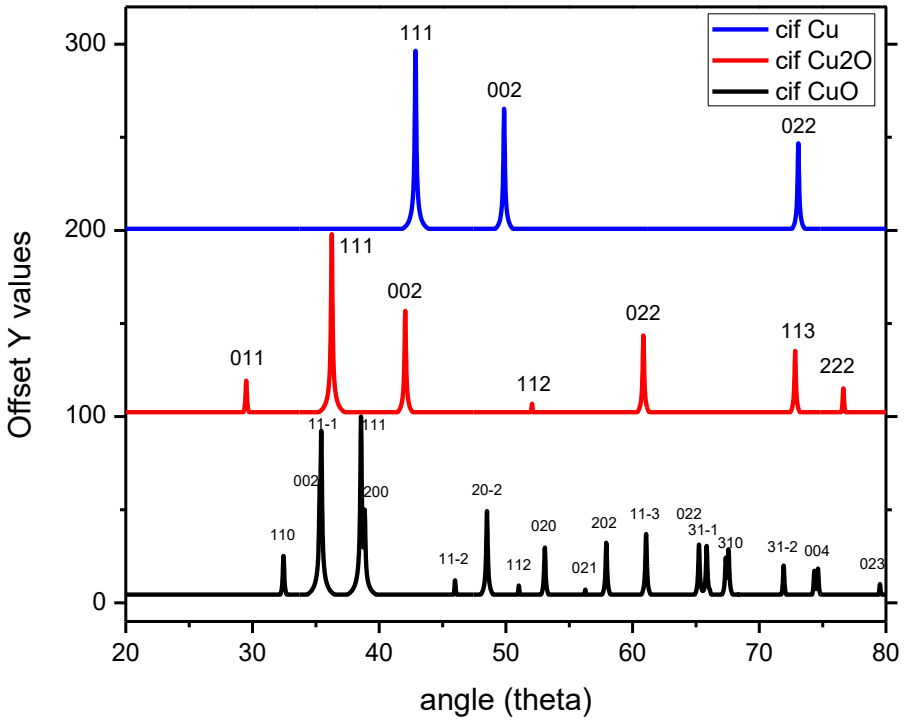

Figure 4.3: XRD analysis of the Cu, CuO, Cu_2O cif files

The XRD data of copper oxide on glass substrate grown by spin coating technique revealed both CuO and Cu_2O in the sample (figure 4.4). This sample exhibits the CuO peaks at (110), (200), (20-2), (020), (202), (11-3), (31-1), (220), (311) and (004) plane with only one Cu_2O peak present at (111) plane. From the XRD peaks, it can be said that the sample had preferential growth on (111) and (200) planes. The XRD data of the ITO substrate reveals its peaks at 21.69^0, 25.91^0, 30.68^0, 35.58^0, 37.78^0, 51.0^0, and 60.79^0 position (figure 4.5).

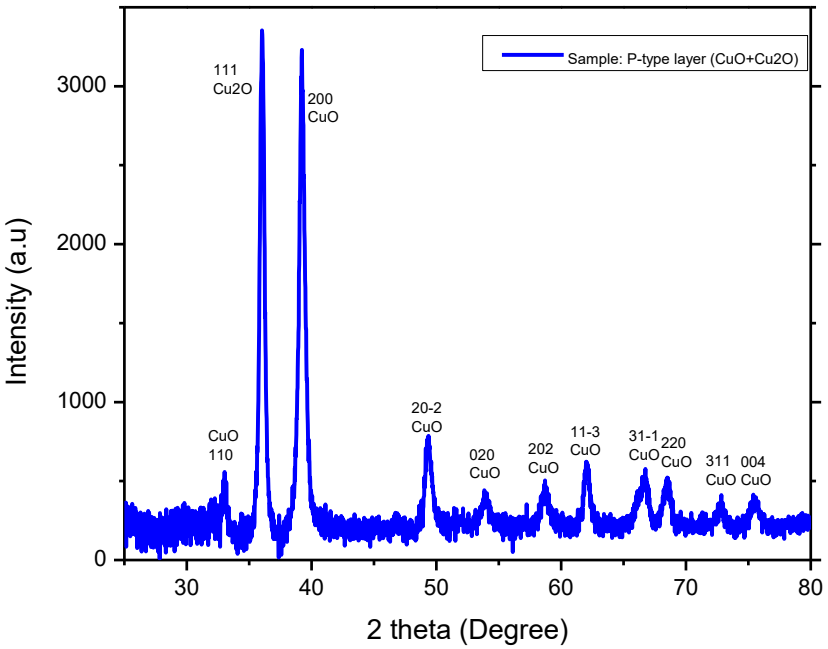

Figure 4.4: XRD analysis of the spin coated CuO layer on glass substrate.

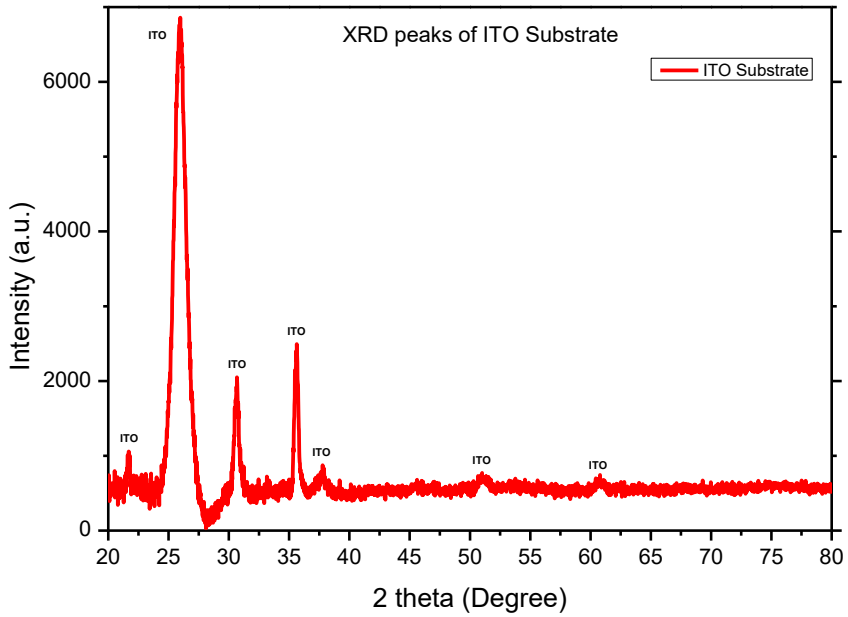

Figure 4.5: XRD analysis of the ITO on glass substrate.

The XRD data from figure 4.6 represents the TiO_2 sample grown on glass/ITO substrate. In the figure, S stands for the substrate ITO, “T” stands for the titanium, “A” stands for anatase, and “R” stands for the rutile phase of the TiO_2. It reveals that the sample had the ITO peaks present in it, which matches the previous XRD peaks. The sample has TiO_2 peaks at R(200), and R(210) which represent the rutile phase and peaks at A(200), A(105) and A(204) represent the anatase phase of TiO_2 matching the literature.[42–47] So, it can be easily concluded that the TiO_2 sample grown on ITO has a mixture of rutile and anatase phase present in it. It also has a very little titanium peak at (101) plane.

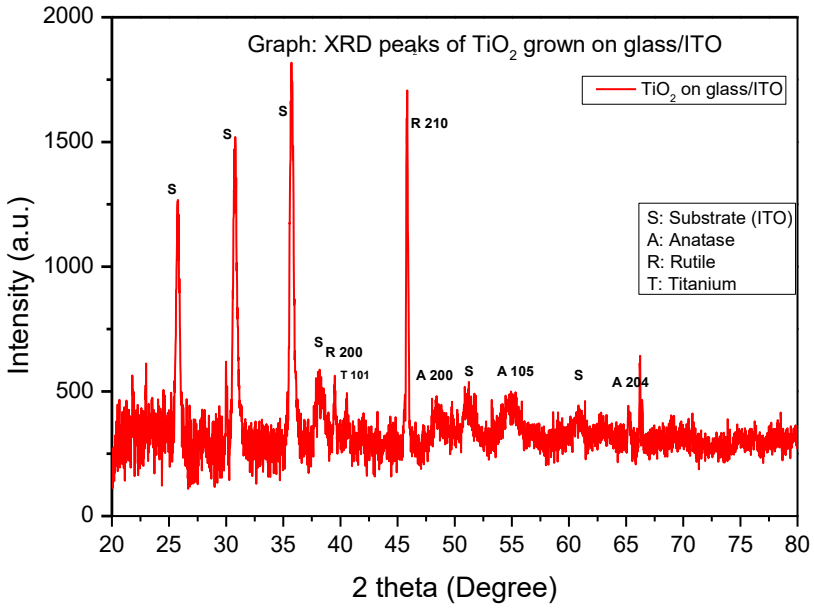

.

Figure 4.6: XRD analysis of the glass/ITO/TiO_2 layer

The following XRD analysis was performed on a complete fabricated solar cell sample which is shown in the figure 4.7. The XRD data shows diffraction peaks for the ITO

substrate which is represented by "S" in the figure. The sample has TiO_2, CuO, and Cu_2O peaks present in it too. The peak positions and hkl values match the previously discussed ITO, TiO_2, CuO and Cu_2O peaks.

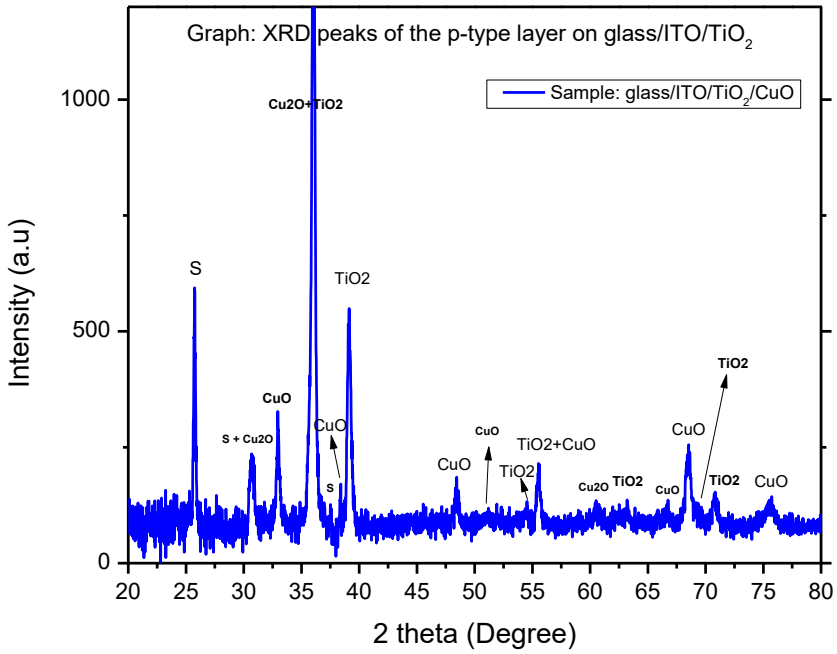

Figure 4.7: XRD analysis of the complete glass/ITO/TiO_2/CuO solar cell

Raman Spectroscopy

Based on the molecular vibration and crystal structure, any Raman active material can be used to study the molecular level structural properties. Using this method very subtle changes in the crystallinity as well as presence of impurity atoms, doping effect, and surface disorder can be verified.[48] This characterization method is non-destructive and non-contact. This does not take much preparation of the sample and any state of the material i.e., gas, liquid and solid can be used for Raman spectroscopy. Figure 4.8 shows the Raman spectroscopy of PLD grown TiO_2

samples on quartz substrates. The figure exhibits Raman peaks around 134 cm^{-1}, 229 cm^{-1}, 434 cm^{-1}, and 600 cm^{-1} that matches with literature peaks.[49,50] These peaks indicate the presence of TiO_2 in the quartz substrate. The peaks around 434 cm^{-1}, and 600 cm^{-1} have lower intensity than the peak around 134 cm^{-1}. This clarifies the dominant presence of rutile phase than the anatase phase in the samples. The figure 4.9 represents the Raman spectroscopy of the PLD grown TiO_2 samples on ITO substrates. In the figure, the bottom black graph shows the Raman spectroscopy of glass/ITO substrate. The above four-line graphs represent four different glass/ITO/TiO_2/CuO samples. It is clearly seen that, on the glass/ITO/TiO_2 samples the peaks near 134 cm^{-1}, 229 cm^{-1}, 434 cm^{-1}, and 600 cm^{-1} have way higher intensity compared to the glass/ITO graph. It clearly indicates that the solar samples have presence of TiO_2.

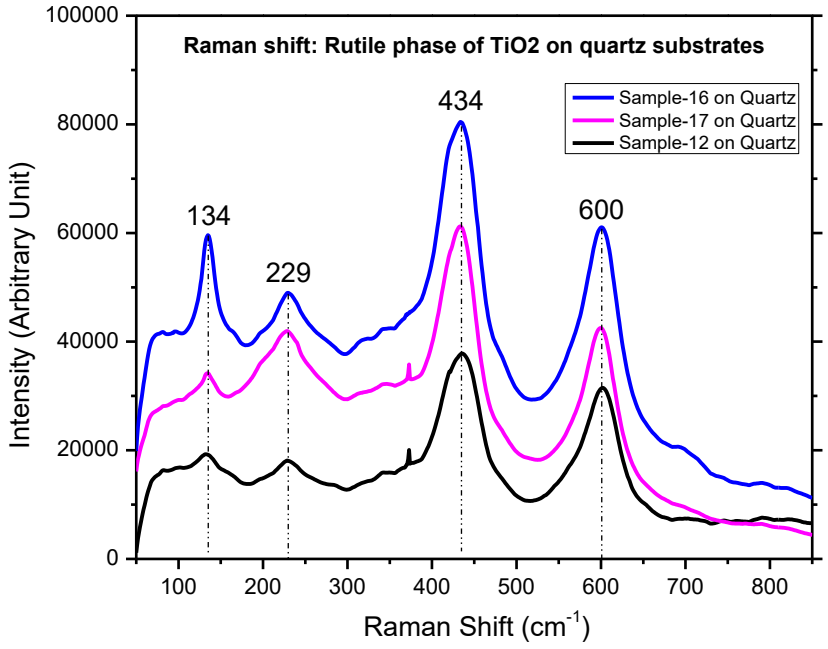

Figure 4.8: Raman spectroscopy of the PLD grown TiO2 samples on quartz substrate.

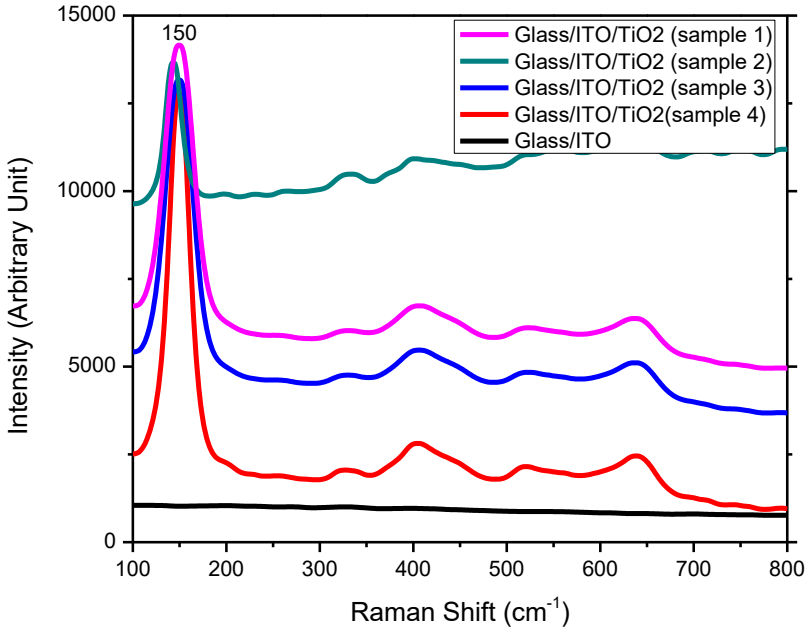

Figure 4.9: Raman spectroscopy of the PLD grown TiO_2 samples on ITO

Electrical Properties

For the electrical measurements Keithley 4200-scs parameter analyzer was used. Newport power supply and HR4000 high-resolution spectrometer was used to perform the diode characteristics under solar spectrum and dark. The following diagram (figure 4.10) shows the top and the bottom contact of the solar cell sample connected with two probes in the probe station and being tested by the Keithley 4200-scs parameter analyzer.

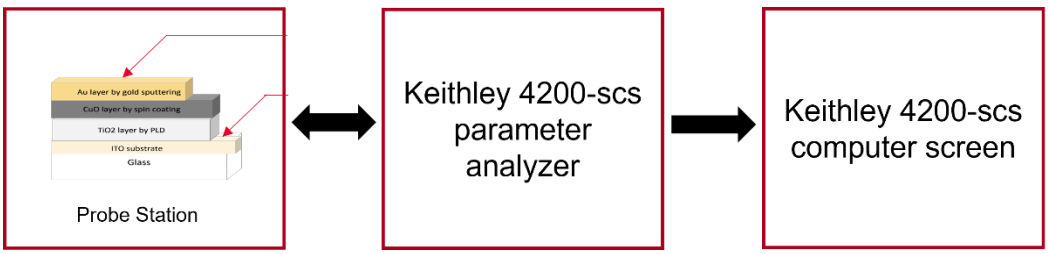

Figure 4.10: Electrical measurement setup diagram. (Components are not to scale.)

Diode characterization was performed on the solar cell samples to check their performance. Three different type of solar cell samples were tested by this system.

Type 1: the TiO_2 layer was grown by PLD and the CuO layer was grown by spin coating.
Type 2: both the layers are grown by pulsed laser deposition.
Type 3: both the layers are PLD grown followed by another spin coating layer of CuO.

The figure 4.11 shows the diode characteristics of a standard diode. The current vs voltage measurement shows that there is almost no current when negative voltage is applied while a sudden increase of current can be seen when the positive voltage is applied under a voltage range from -1v to +1v. Figure 4.12 shows the I-V measurement of the type 1 solar cell where the TiO_2 layer was deposited by PLD, and the CuO layer was deposited by spin coating. The figure shows the diode characteristics test from -1v to +1v. The graph shows symmetric curve on the positive and negative side of 0 V which refers to the fact that the solar cell was shorted.

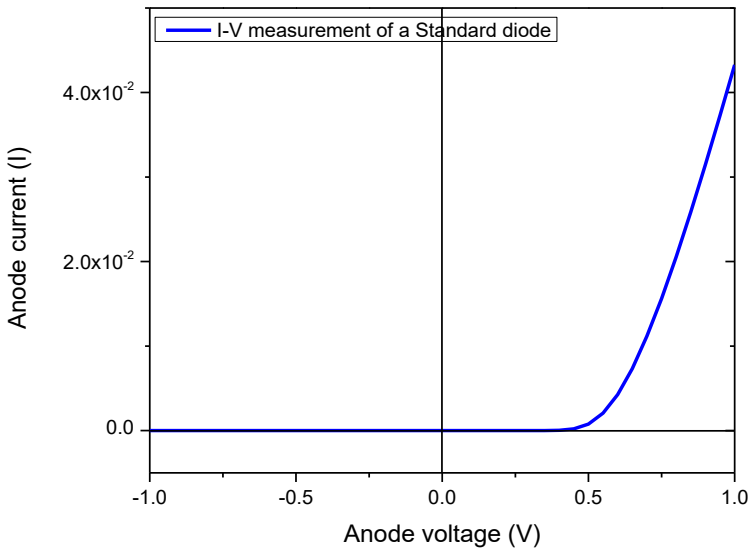

Figure 4.11: Standard diode characteristics (I-V measurement)

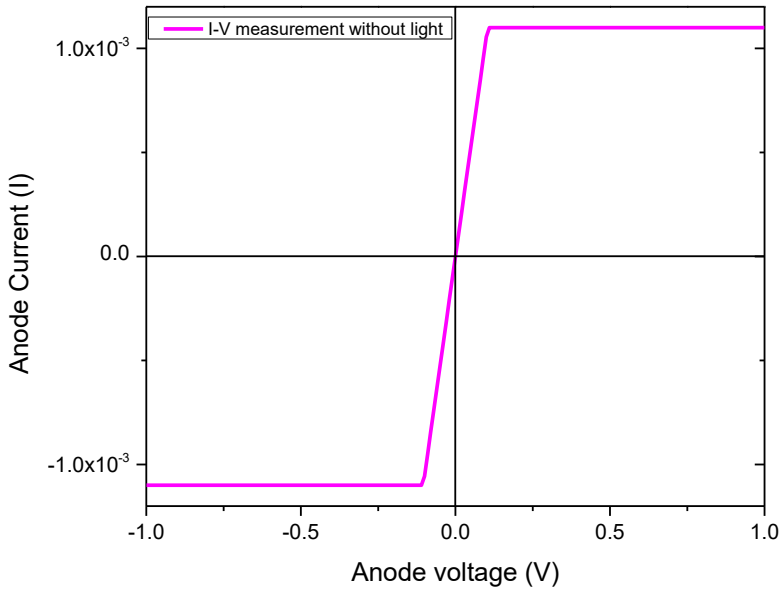

Figure 4.12: Diode characteristics (I-V) measurement of the solar cell (Type 1 Sample)

The figure 4.13 shows the I-V measurements performed on the type 2 samples where the TiO_2 and the CuO both layers were deposited by PLD. Both the graphs show I-V measurement from -1v to +1v range. It is observed that the graph is asymmetric positive and negative voltage sides which refers to a diode like character of the sample. The measurement was done with light and no light to observe the effect of light. Under light, the graph was shifted downwards on the positive voltage and upwards on the negative voltage. This concludes that the sample had diode like behavior, and it reacts upon the exposure of light.

Figure 4.14 represents the same type 2 sample, but this time the characteristic is more diode like and upon exposure of sun light the full graph is shifted downwards which indicated solar cell characteristic.

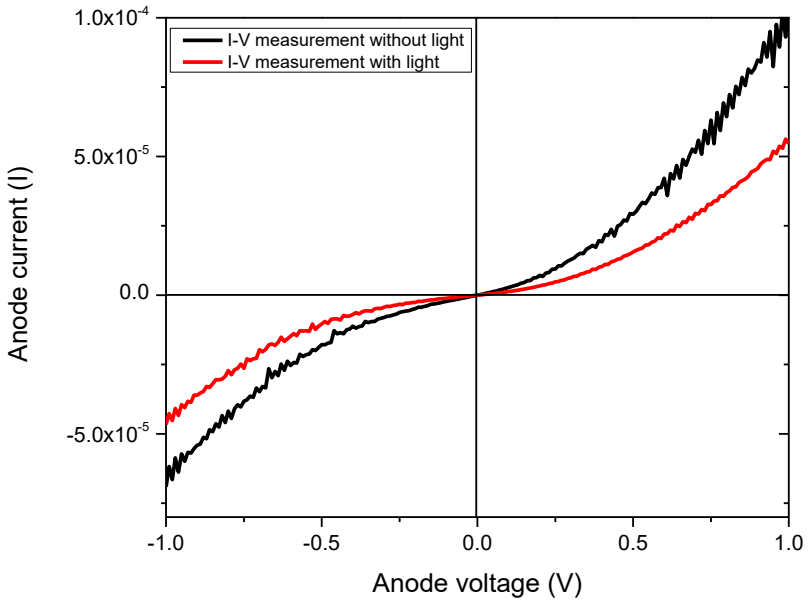

Figure 4.13: Diode characteristics (I-V) measurement of the solar cell (Type 2 Sample)

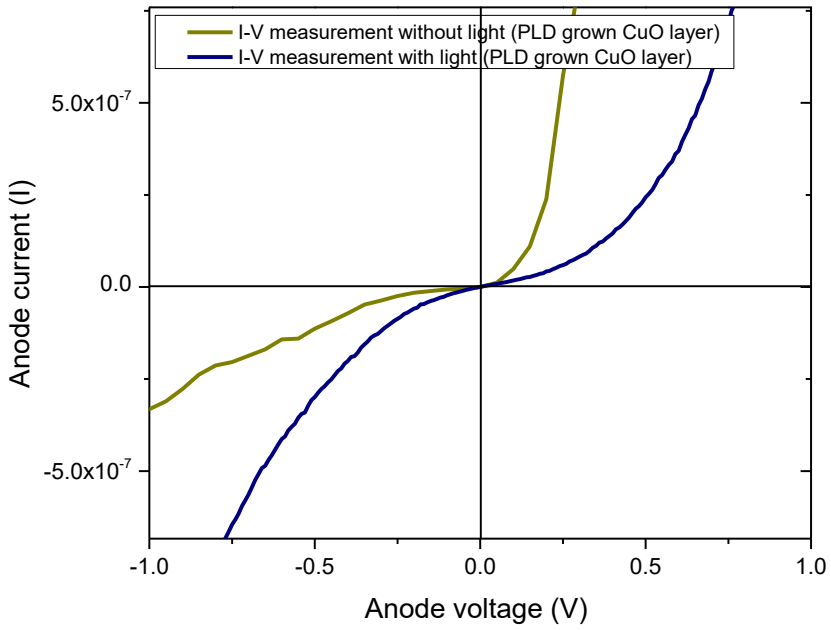

Figure 4.14: Diode characteristics (I-V) measurement of the solar cell (Type 2 Sample)

The figure 4.15 showed the best result under the range from -1v to +1v. The top graph, the I-V test for the diode characteristics, clearly shows diode behavior. Upon exposure of light, the graph is completely shifted downwards showing solar cell characteristics. There is a small region of open circuit voltage and short circuit current.

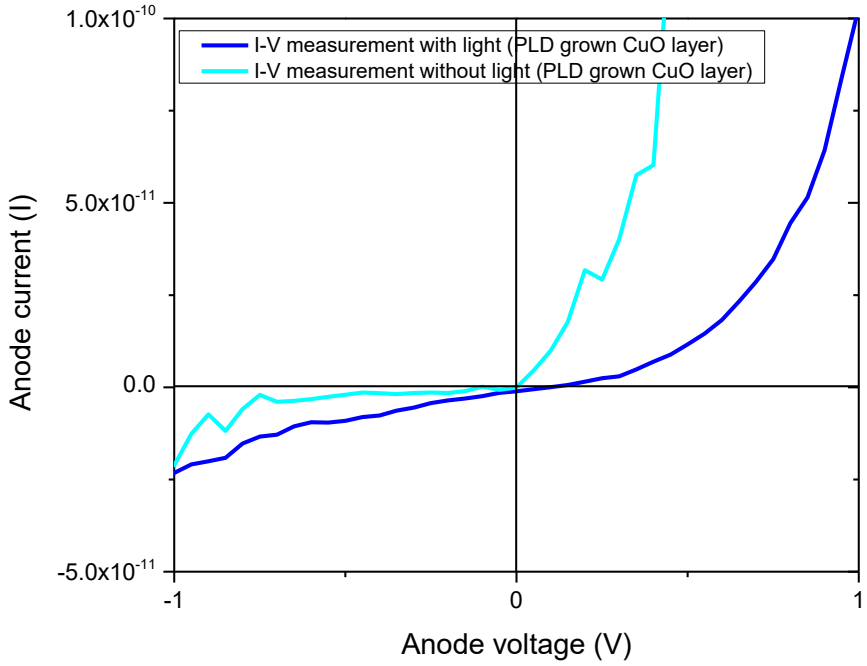

Figure 4.15: Diode characteristics (I-V) measurement of the solar cell (Type 2 Sample)

The figure 4.16 shows similar sample and similar result on the I-V test. The sample clearly showed diode characteristics, and the graph shifted downward while under illumination showing the solar cell characteristics. This sample also has a small area under the V_{oc} and I_{sc} region showing the efficiency of the solar cell.

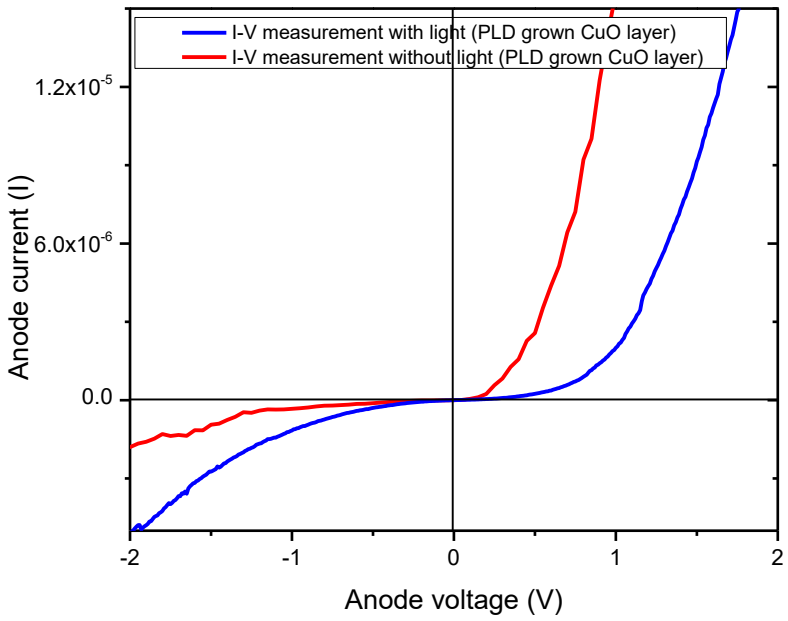

Figure 4.16: Diode characteristics (I-V) measurement of the solar cell (Type 2 Sample)

Figure 4.17 and figure 4.18 are the solar characteristics of the type 3 samples where the TiO_2 and CuO layers were deposited by PLD followed by a spin coating layer of CuO. The first figure shows the I-V curve from -1v to +1.5v and the second figure shows a range of -1v to +1v. From both figures the diode characteristics of the fabricated solar cell is obvious, but upon light exposure the curve is only shifted downwards on the positive voltage region. This explains that the samples may have solar like behavior but from this time of graph it is clearly not acting as a solar cell and the efficiency cannot be calculated.

SEM-EDS Analysis

Scanning electron microscopy (SEM) and energy dispersive X-ray spectroscopy (EDS or EDX) are the techniques to analyze the surface topology, surface morphology, and elemental composition of a sample. In SEM electron beam incidents on a sample that ejects electrons from

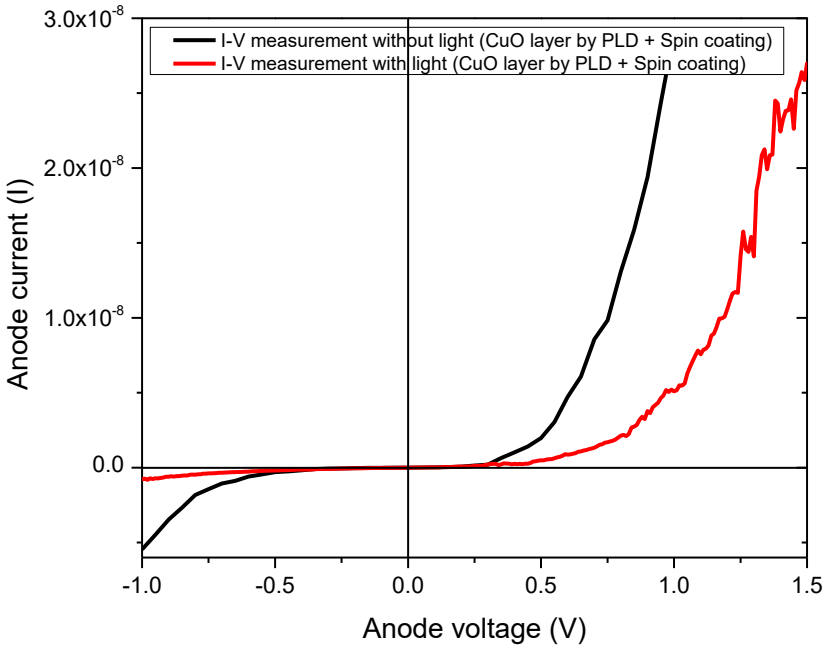

Figure 4.17: Diode characteristics (I-V) measurement of the solar cell (Type 3 Sample)

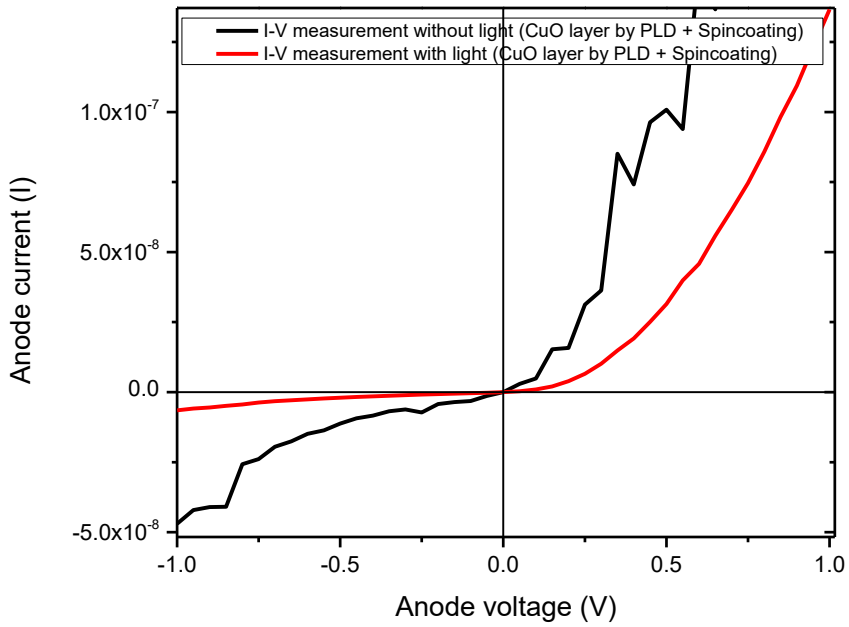

Figure 4.18: Diode characteristics (I-V) measurement of the solar cell (Type 3 Sample)

the atoms present on the samples surface. This creates electron vacancies that are filled with higher state electrons. To balance this energy difference of two different states, x-rays are emitted. Different type of element emits different type of energy that is called the characteristics of that element. The relative abundance of the emitted x-rays from the sample versus their energy is detected by the EDS detector. This paves the way to do elemental composition of the sample surface. The SEM-EDS analysis was performed on the solar cell samples in FEI FESEM Quanta-200F integrated with an enhanced EDS detector facility.

The figure 4.19 shows the morphology of the type 2 samples. The SEM image shows that the surface is smooth, and there is no trace of particulate or agglomerated materials on the surface. Figure 4.20 shows the EDS images of the PLD grown solar cell. It is observed that the sample has nicely distributed presence of all the materials.

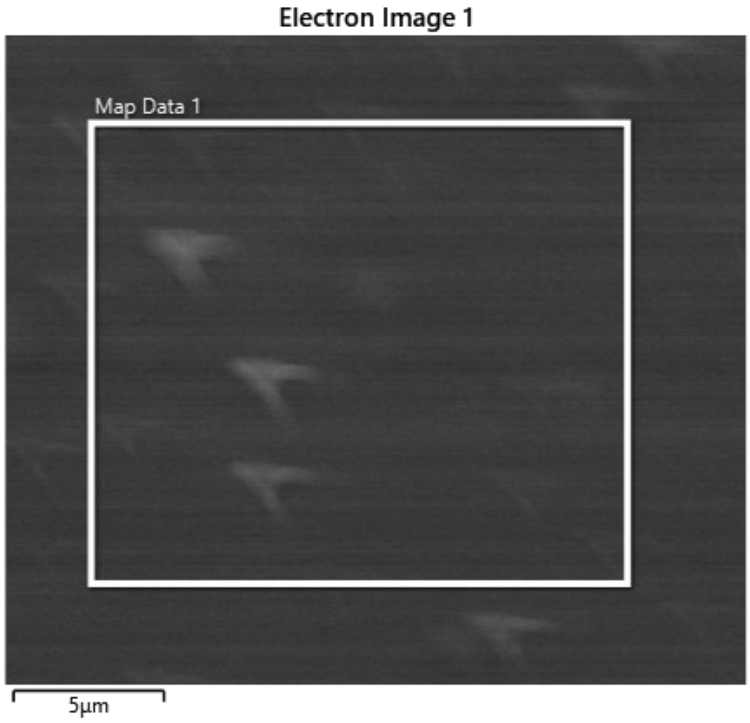

Figure 4.19: SEM image of PLD grown solar cell (type 2 sample)

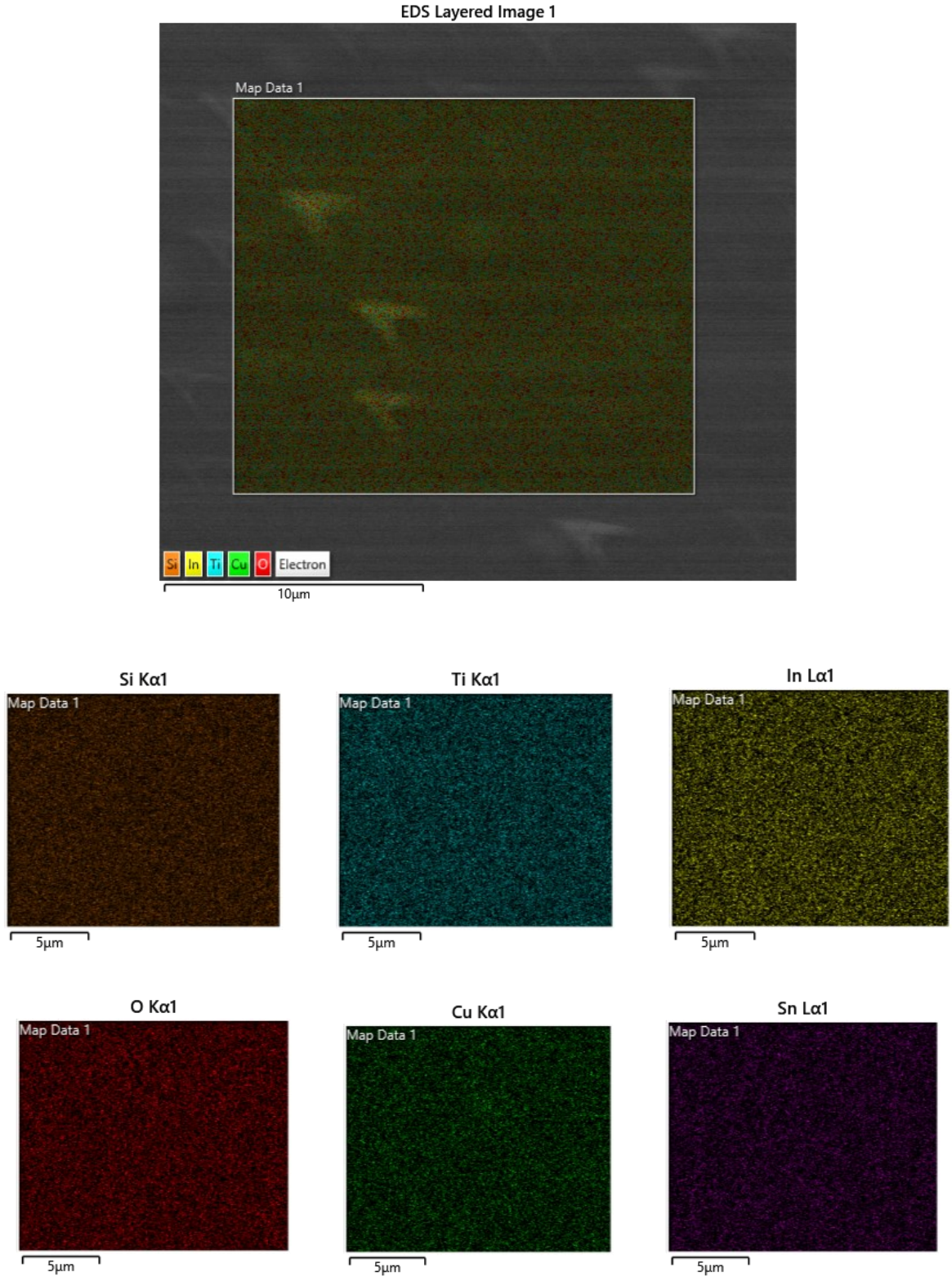

Figure 4.20: EDS image of the PLD grown solar cell showing the distributed presence of all the materials

The figure 4.21 is the visual representation of the EDS data of the solar cell sample. In this figure 4.21, it is observed that all the materials present in the sample showed peaks in the graph of the EDS data.

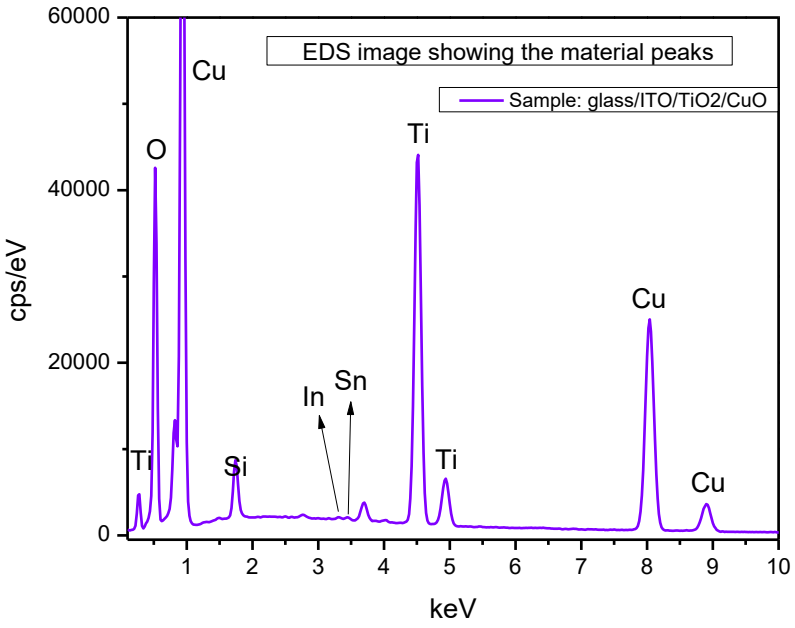

Figure 4.21: EDS data showing the presence of all the materials in the sample.

The following figure 4.22 shows the SEM image of a solar cell sample where all the layers were fabricated by PLD, and a CuO layer was deposited by spin coating on top of that. The image shows the CuO particles with the background of PLD grown CuO layer. It is observed that the spin coating could not evenly spread the material, and the size of the particle is also not same. In some places there are more particles than the other which can be a cause of the lower performance of the type 3 solar cell.

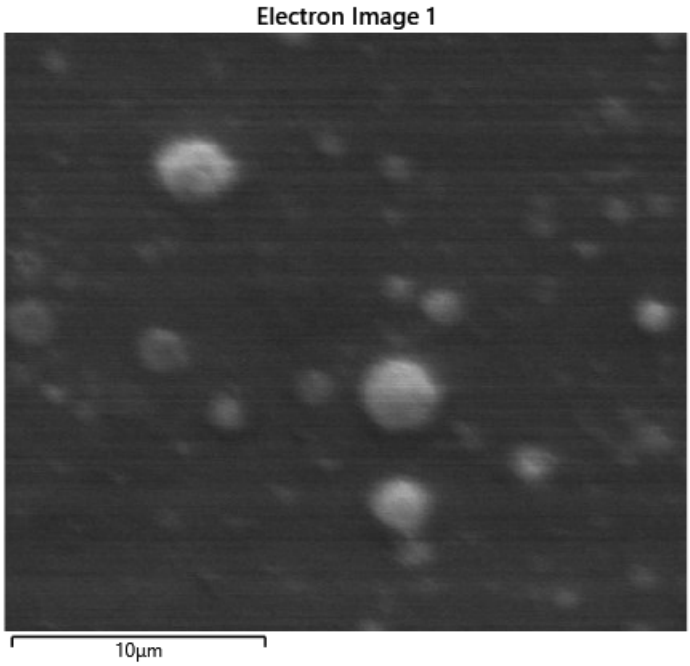

Figure 4.22: SEM image of PLD grown solar cell with a CuO spin coated layer (type 3 sample)

The figure 4.23 shows the EDS images of the type 3 solar cell sample. In the figure, the presence of all the materials i.e., Cu, Ti, O, Si, In, and Sn can be observed in the solar cell sample.

UV-VIS Spectroscopy

For the UV-VIS, newport power supply and HR4000 high-resolution spectrometer was used and operated with the Oceanview software. The following three figures (figure 4.24, figure 4.25, figure 4.26) show the UV visible transmittance spectroscopy for the above mentioned three types of samples.

First the pristine spectrum was taken to use as the reference which is the black graph. Then the glass/ITO substrate's transmittance data was taken which is the red graph in the figures. It shows that the glass/ITO transmits most of the visible light spectra through it. The blue one is

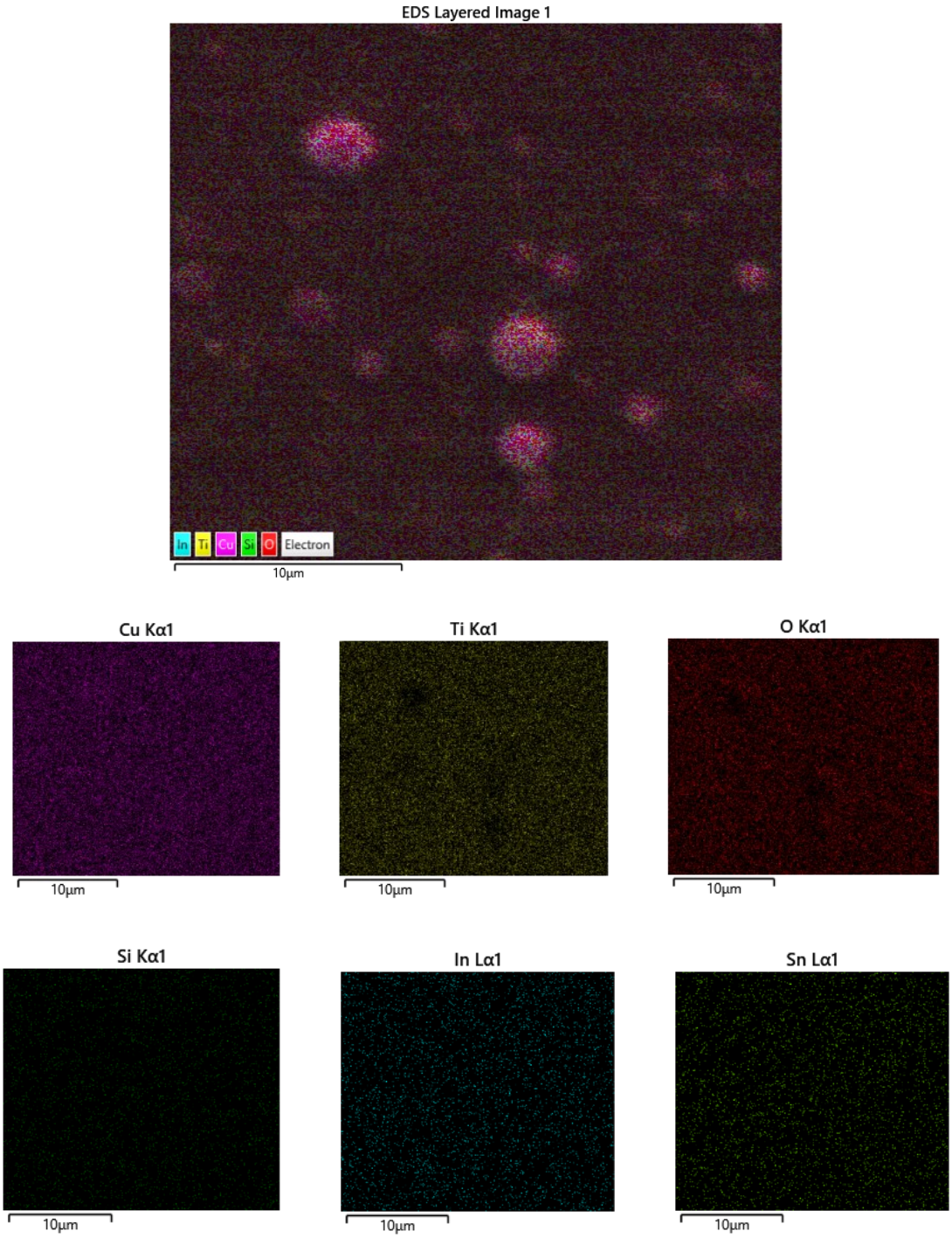

Figure 4.23: EDS image of PLD grown solar cell with a CuO spin coated layer (type 3 sample) showing the distributed presence of all the materials

the glass/ITO/TiO_2 data that represents how most of the visible spectra is transmitted through this TiO_2 window layer. As the TiO_2 is the window layer, this agrees with the theoretical expectation.

Finally, the blue graph shows the CuO layer which tells us that most of the visible light spectra from 400 nm to 750 nm is absorbed by this layer and a very little of that spectrum is transmitted. The lesser the transmitted spectra through this CuO, the absorber layer, the better the optoelectronic properties of a solar cell should be.

Comparing figure 4.24 and figure 4.25, it can be clearly seen that the PLD grown CuO layer (type 2 sample) transmits much lesser visible light than the spin coating grown CuO layer (Type 1 sample). Because in the PLD grown sample the CuO layer is nicely spread compared to the spin coating grown sample.

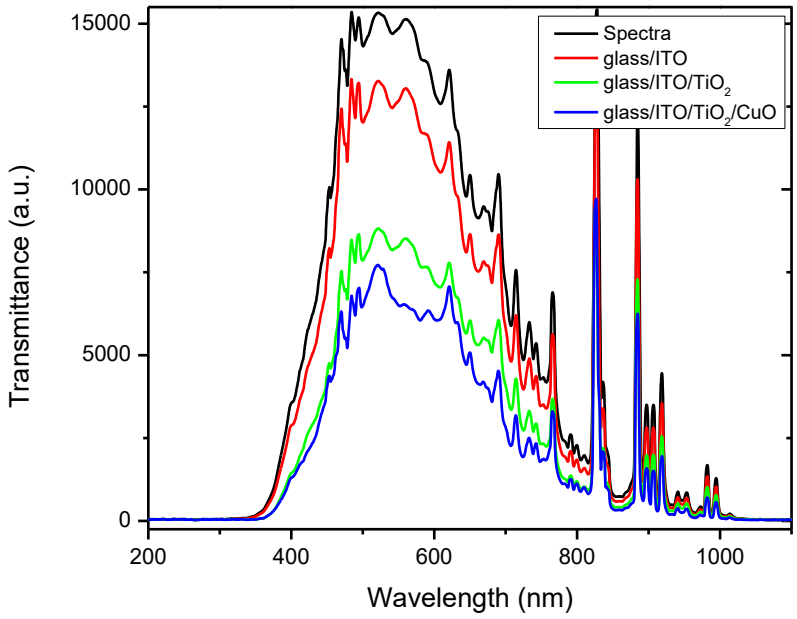

Figure 4.24: UV-VIS spectroscopy comparison between each layer of the glass/ITO/TiO_2/CuO (type 1 sample) solar cell

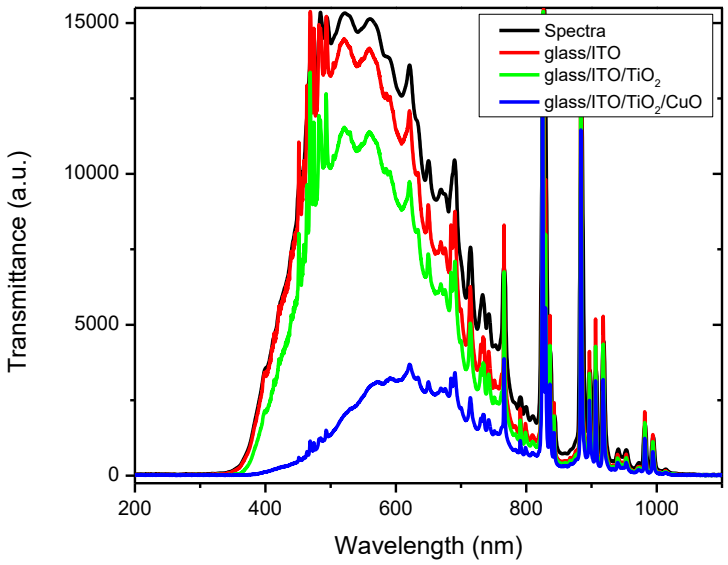

Figure 4.25: UV-VIS spectroscopy comparison between each layer of the glass/ITO/TiO_2/CuO (type 2 sample) solar cell

The same result can be seen (figure 4.26) when the spin coating is done after the PLD for the CuO layer (type 3 sample). There is not much increase in the transmission spectra. So PLD grown CuO sample has more absorbance than spin coating grown CuO sample as an absorber layer. From the transmittance spectra, the absorbance spectra were calculated. The following equation was used to determine the absorbance.

$$A = log_{10}\left(\frac{i}{I}\right) \ldots\ldots\ldots\ldots (1)$$

Where, A= Absorbance

i= Intensity of the light entering the sample (Transmittance of the spectra)

I= Intensity of the light leaving the sample (Transmittance of the samples)

The figure 4.27 shows the calculated absorbance spectra of a (type 3) solar cell samples. The bottom two graphs (black and blue) represent the ITO and ITO/TiO_2 absorbance respectfully.

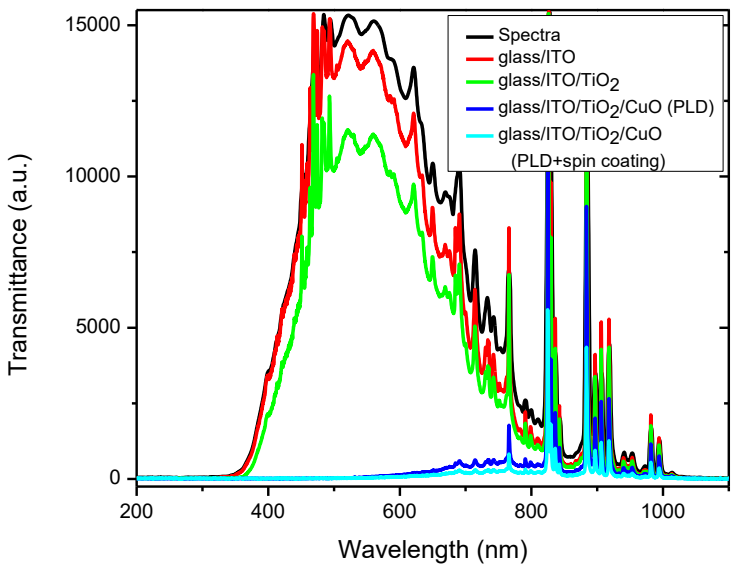

Figure 4.26: UV-VIS spectroscopy comparison between each layer of the glass/ITO/TiO_2/CuO (type 3 sample) solar cell

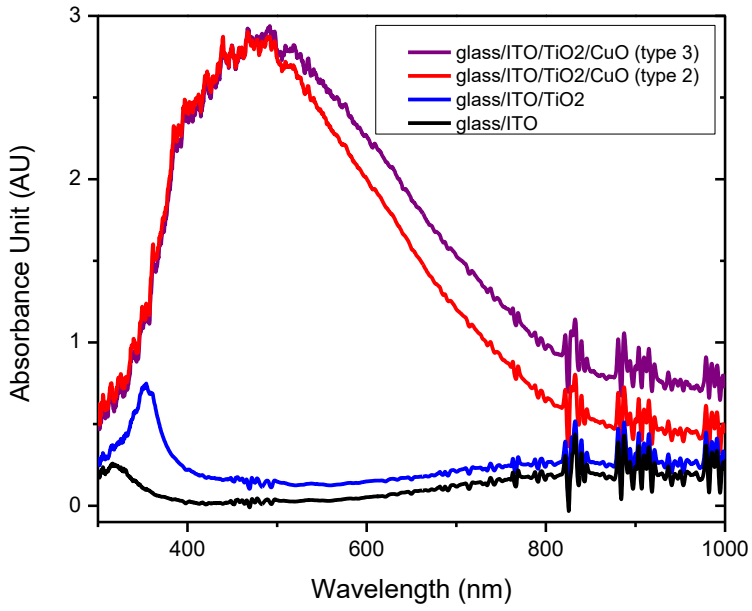

Figure 4.27: Absorbance spectrum of each layer of the solar cell sample

As one is the contact and other is the window layer, they absorb only a little spectrum. The Top two layers (red and purple) absorbs a high number of photons in the visible light region as it is the absorber layer. Again, the spin coated CuO layer (type 3) does not increase much absorbance compared to the PLD grown CuO layer (type 2).

CONCLUSIONS AND FUTURE WORK

The simulation study could successfully finalize TiO_2 as the n-type layer comparing it with ZnO and CuO as the p-type layer comparing it with Cu_2O. The thickness of each of these layers were found through simulation and top and bottom contact was also chosen from the simulation study. This work of simulation reports an efficiency for the solar cell as high as 19.2% with the glass/FTO/TiO_2/CuO/Au heterostructure while the thickness of the TiO_2 and the CuO layer is 1.4µm and 1.2µm respectively. Whereas, with the glass/ITO/TiO_2/CuO/Au heterostructure, replacing FTO with ITO gives an efficiency as high as 11.5% for the solar cell. The experimental work followed the simulation results. This work could successfully grow the individual layers of the solar cell which is TiO_2 and CuO on different substrates i.e., glass, quartz, and ITO. The complete glass/ITO/TiO_2/CuO solar cell was fabricated using PLD, spin coating and sputtering technique and characterized with XRD and Raman spectroscopy that proved the presence of rutile phase of TiO_2 for the window layer and a mixture of CuO and Cu_2O for the active layer. The I-V measurement showed the diode characteristics for the solar samples. It was observed that the PLD grown samples worked best and performed better than those samples where spin coating was used to grow the absorber layer of CuO. The surface morphology was discussed with SEM-EDS, and the UV-VIS showed the solar cell layer light absorbance and transmittance. In future, FTO can be used as the bottom contact to fabricate solar cell and efficiency can be measured and compared with the ones where ITO was used. This efficiency measurement can be compared with the simulation-based study that showed FTO has better performance than that of ITO. Also, a phase mixture of CuO and Cu_2O can be studied experimentally to increase the optoelectronic properties hence efficiency of the solar cell.

REFERENCES

[1] S. Hussain, C. Cao, Z. Usman, Z. Chen, G. Nabi, W.S. Khan, Z. Ali, F.K. Butt, T. Mahmood, Thin Solid Films 522 (2012) 430–434.

[2] Z. Starowicz, G. Wisz, R. Yavorskyi, Z. Zapukhlyak, M. Bester, Ł. G, (2019).

[3] A. Bhaumik, A. Haque, P. Karnati, M.F.N. Taufique, R. Patel, K. Ghosh, Thin Solid Films 572 (2014) 126–133.

[4] M. Grätzel, Nature 421 (2003) 586–587.

[5] T. Markvart, L. Castaner, Solar Cells Materials: Manufacture and Operation, Elsevier, Oxford, 2005.

[6] S. Agarkar, V. Dhas, S. Muduli, S. Ogale, RSC Adv. 2 (2012) 11645–11649.

[7] M. Pavan, S. Rühle, A. Ginsburg, D.A. Keller, H.N. Barad, P.M. Sberna, D. Nunes, R. Martins, A.Y. Anderson, A. Zaban, E. Fortunato, Sol. Energy Mater. Sol. Cells 132 (2015) 549–556.

[8] R. Jose, V. Thavasi, S. Ramakrishna, J. Am. Ceram. Soc. 92 (2009) 289–301.

[9] T. Oekermann, D. Zhang, T. Yoshida, H. Minoura, J. Phys. Chem. B 108 (2004) 2227–2235.

[10] S. Murugesan, P. Kuppusami, N. Parvathavarthini, E. Mohandas, Surf. Coatings Technol. 201 (2007) 7713–7719.

[11] S.N. Mazhir, N.H. Harb, IOSR J. Appl. Phys. 7 (2015) 14–21.

[12] E. György, G. Socol, E. Axente, I.N. Mihailescu, C. Ducu, S. Ciuca, Appl. Surf. Sci. 247 (2005) 429–433.

[13] S. iti Kitazawa, Y. Choi, S. Yamamoto, T. Yamaki, Thin Solid Films 515 (2006) 1901–1904.

[14] Y. Choi, S. Yamamoto, T. Umebayashi, M. Yoshikawa, Solid State Ionics 172 (2004) 105–108.

[15] B.P. Rai, Sol. Cells 25, 1988.

[16] T. Minami, T. Miyata, K. Ihara, Y. Minamino, S. Tsukada, Thin Solid Films 494 (2006) 47–52.

[17] K. Akimoto, S. Ishizuka, M. Yanagita, Y. Nawa, G.K. Paul, T. Sakurai, 715 (2006).

[18] M. Izaki, K. Mizuno, T. Shinagawa, M. Inaba, A. Tasaka, J. Electrochem. Soc. 153 (2006) C668.

[19] V. Figueiredo, E. Elangovan, G. Gonçalves, P. Barquinha, L. Pereira, N. Franco, E. Alves, R. Martins, E. Fortunato, Appl. Surf. Sci. 254 (2008) 3949–3954.

[20] P.A. Korzhavyi, B. Johansson, Swedish Nucl. Fuel Waste Manag. Co. (2011).

[21] A.H. Jayatissa, K. Guo, A.C. Jayasuriya, Appl. Surf. Sci. 255 (2009) 9474–9479.

[22] R.H. Bari, S.B. Patil, A.R. Bari, Int. Nano Lett. 3 (2013) 2–6.

[23] Ş. Korkmaz, B. Geçici, S.D. Korkmaz, R. Mohammadigharehbagh, S. Pat, S. Özen, V. Şenay, H.H. Yudar, Vacuum 131 (2016) 142–146.

[24] T.V. Pham, M. Rao, P. Andreasson, Y. Peng, J. Wang, K.B. Jinesh, Appl. Phys. Lett. 102 (2013) 2–6.

[25] M. Heinemann, B. Eifert, C. Heiliger, Phys. Rev. B - Condens. Matter Mater. Phys. 87 (2013) 3–7.

[26] N. Serin, T. Serin, Ş. Horzum, Y. Çelik, Semicond. Sci. Technol. 20 (2005) 398–401.

[27] A. Mittiga, E. Salza, F. Sarto, M. Tucci, R. Vasanthi, Appl. Phys. Lett. 88 (2006) 16–18.

[28] H. Kidowaki, T. Oku, T. Akiyama, A. Suzuki, B. Jeyadevan, J. Cuya, J. Mater. Sci. Res. 1 (2011).

[29] Z.Y. Fan, H. Razavi, J.W. Do, A. Moriwaki, O. Ergen, Y.L. Chueh, P.W. Leu, J.C. Ho, T. Takahashi, L.A. Reichertz, S. Neale, K. Yu, M. Wu, J.W. Ager, A. Javey, Nat. Mater. 8 (2009) 648–653.

[30] B.M. Kayes, H.A. Atwater, N.S. Lewis, J. Appl. Phys. 97 (2005).

[31] J.A. Czaban, D.A. Thompson, R.R. Lapierre, Nano Lett. 9 (2009) 148–154.

[32] E.C. Garnett, P. Yang, J. Am. Chem. Soc. 130 (2008) 9224–9225.

[33] R. Asahi, T. Morikawa, T. Ohwaki, K. Aoki, Y. Taga, Science (80-.). 293 (2001) 269–271.

[34] B.W. Faughnan, R.S. Crandall, Appl. Phys. Lett. 31 (1977) 834–836.

[35] L.M. Wong, S.Y. Chiam, J.Q. Huang, S.J. Wang, J.S. Pan, W.K. Chim, J. Appl. Phys. 108

(2010) 0–6.

[36] T. Islam, R. Jani, S.M. Al Amin, K.M. Shorowordi, S.S. Nishat, A. Kabir, M.F.N. Taufique, S. Chowdhury, S. Banerjee, S. Ahmed, Comput. Mater. Sci. 184 (2020).

[37] M.R. Jani, M.T. Islam, S.M. Al Amin, M.S. Us Sami, K.M. Shorowordi, M.I. Hossain, S. Chowdhury, S.S. Nishat, S. Ahmed, Superlattices Microstruct. 146 (2020) 106652.

[38] H. Du, W. Wang, Z. Zhu, F. Wu, Q. Qiao, S. Huang, Q. Li, (2018) 0–10.

[39] C.F. Smura, D.R. Parker, M. Zbiri, M.R. Johnson, Z.A. Gál, S.J. Clarke, J. Am. Chem. Soc. 133 (2011) 2691–2705.

[40] F. Pr, C. Cu, S. Untersuchung, D. Aufnahmen, D. Korrektion, U. Voraussetzung, (1930) 845–850.

[41] G. Tunell, E. Posnjak, C.J. Ksanda, Zeitschrift Für Krist. - Cryst. Mater. 90 (1935) 120–142.

[42] X. Liu, X.Y. Chen, J. Yin, Z.G. Liu, J.M. Liu, X.B. Yin, G.X. Chen, M. Wang, J. Vac. Sci. Technol. A Vacuum, Surfaces, Film. 19 (2001) 391–393.

[43] S.S. Al-obaidi, A.A. Yousif, 26 (2013).

[44] X.S. Zhou, Y.H. Lin, B. Li, L.J. Li, J.P. Zhou, C.W. Nan, J. Phys. D. Appl. Phys. 39 (2006) 558–562.

[45] E. György, A. Pérez Del Pino, G. Sauthier, A. Figueras, F. Alsina, J. Pascual, J. Phys. D. Appl. Phys. 40 (2007) 5246–5251.

[46] C. Garapon, C. Champeaux, J. Mugnier, G. Panczer, P. Marchet, A. Catherinot, B. Jacquier, Appl. Surf. Sci. 96–98 (1996) 836–841.

[47] X. Liu, J. Yin, Z.G. Liu, X.B. Yin, G.X. Chen, M. Wang, Appl. Surf. Sci. 174 (2001) 35–39.

[48] M. Silambarasan, S. Saravanan, T. Soga, Phys. E Low-Dimensional Syst. Nanostructures 71 (2015) 109–116.

[49] L. Escobar-Alarcón, E. Haro-Poniatowski, M.A. Camacho-López, M. Fernández-Guasti, J. Jímenez-Jarquín, A. Sánchez-Pineda, Appl. Surf. Sci. 137 (1999) 38–44.

[50] G. Shukla, P.K. Mishra, A. Khare, J. Alloys Compd. 489 (2010) 246–251.